# Modulation of premotor cortex excitability mitigates the behavioral and electrophysiological abnormalities in a Parkinson's Disease Mouse Model

In Sun Choi[1,2], Jinmo Kim[3], Joon Ho Choi[1], Ji-Woong Choi[2,3,†], and Jong-Cheol Rah[1,2,4,†*]

[1]Laboratory of Neurophysiology, Sensory and Motor Neuroscience Group, Korea Brain Research Institute, Daegu, 41602, Republic of Korea.

[2]Brain Engineering Convergence Research Center, Daegu Gyeongbuk Institute of Science and Technology (DGIST), Daegu, 42988, Republic of Korea.

[3]Department of Electrical Engineering and Computer Science, DGIST, Daegu, 42988, Republic of Korea.

[4]Department of Brain Sciences, DGIST, Daegu, 42988, Republic of Korea.

[†]These authors contributed equally to this work as last authors.

*Jong-Cheol Rah

Sensory and Motor Neuroscience Group, Korea Brain Research Institute, 61 Cheomdan-ro, Dong-gu, Daegu, 41062, Republic of Korea

**Phone number:** 82-53-980-8350

**Email:** jcrah@kbri.re.kr

**Author Contributions:** Study design: J-CR; ISC, data gathering and analysis: ISC; further analysis of the *in-vivo* electrophysiology data: JMK; project supervision: J-CR, JWC; writing: all authors contributed.

**Competing Interest Statement:** Authors declare that they have no competing interests.

**Classification:** Biological Sciences

**Keywords:** Parkinson’s disease; subthalamic nucleus; premotor cortex; deep brain stimulation; HCN channel

**This PDF file includes:**

Main Text
Figures 1 to 7

**Abstract**

The subthalamic nucleus (STN) is important in halting ongoing behaviors, referred to as stop-signal responses. The prefrontal regions innervating the STN exhibit increased activity during the stop-signal responses, and optogenetic activation of these neurons inhibits impulsive actions in rodents. High-frequency electrical stimulation of the STN effectively treats motor symptoms of Parkinson's disease (PD), yet its underlying circuit mechanisms are unclear. Here, we investigated the involvement of STN-projecting premotor (M2) neurons in PD mouse models and the impact of deep brain stimulation targeting the STN (DBS-STN). We found that M2 neurons exhibited enhanced burst firing and synchronous oscillations in the PD mouse model. Remarkably, high-frequency stimulation of STN-projecting M2 neurons, simulating antidromic activation, during DBS-STN relieved motor symptoms and hyperexcitability. These changes were attributed to reduced firing frequency vs. current relationship through normalized hyperpolarization-activated inward current ($I_h$). The M2 neurons in the PD model mouse displayed increased $I_h$, which was reversed by high-frequency stimulation. Additionally, the infusion of ZD7288, an HCN channel blocker, into the M2 replicated the effects of high-frequency stimulation. In conclusion, our study unveils excessive excitability and suppressive motor control through M2-STN synapses in the PD mouse model. Antidromic excitation of M2 neurons during deep brain stimulation of the STN alleviates this suppression, thereby improving motor impairment. These findings provide insights into the circuit-level dynamics underlying deep brain stimulation's therapeutic effects in PD. Targeting M2-STN synapses may be useful for future therapeutic strategies.

**Significance Statement**

Our study provides insight into the mechanisms driving motor impairment in Parkinson's disease (PD) and the therapeutic efficacy of deep brain stimulation (DBS). By elucidating the role of hyperpolarization-activated cyclic nucleotide-gated (HCN) channels in modulating the hyperexcitability of M2 neurons, we identify potential targets for future PD treatment strategies. Understanding the excessive excitability and suppressive motor control through M2-STN synapses in PD mouse models contributes to our knowledge of circuit-level dynamics underlying DBS effects. These findings have significant implications for improving motor symptoms and advancing the development of more precise and effective interventions for PD patients.

## Main Text

### Introduction

The balance between movement and suppression of movement is finely regulated by corticobasal ganglia pathways (1, 2), and disruption of the balance can lead to motor dysfunctions such as Parkinson's disease (PD) or Huntington's disease. The subthalamic nucleus (STN) transmits glutamatergic projections mainly to the substantia nigra pars reticulata (SNr) and the internal division of the globulus pallidum (GPi), both of which form gamma-aminobutyric acid (GABA)-ergic connections to the motor thalamus (3). The activity of the STN can be predicted to suppress motor thalamocortical connections and, thus, action execution. Indeed, STN activity is involved in stopping or pausing planned or initiated movement across species. STN lesions shortened the reaction time in response to a go signal, increased the level of spontaneous locomotion, and impaired the ability to stop the ongoing movement (2, 4–6). Furthermore, functional removal of the STN improved motor symptoms in PD animal models, such as akinesia and rigidity (7–9). In line with these findings, increased firing of STN neurons has been observed in both PD patients and animal models (10–14).

The exact circuit mechanism of deep brain stimulation on the STN (DBS-STN), an efficient neurosurgical technique used to treat various neurological symptoms in PD, is still under debate (15). However, one explanation is that depletion of the readily releasable pool (RRP) of neurotransmitters by high-frequency stimulation during DBS shuts down the abnormally exaggerated stopping effect of the STN (15, 16). Corroborating this idea, selective RRP depletion of STN axons leads to accelerated locomotor activity (17). However, the origin of the enhanced STN activity in PD remains unclear.

High-order motor cortical areas have been shown to control motor activity cessation in primates. The right inferior frontal gyrus (18, 19) and pre-supplementary motor area (pre-SMA) (20–22) are reported to control motor inhibition via beta-frequency oscillations (23, 24). Repetitive transcranial magnetic stimulation of these areas significantly weakened beta-frequency oscillation, reduced the ability to stop an action, and alleviated motor symptoms in patients (24–26). Interestingly, these areas have strong direct synaptic connections to the STN (27, 28). In rodents, the premotor cortex (M2), involved in motor planning and switching motor plans, projects strongly onto the STN (29). During a task in which mice were trained to initiate or inhibit a motor action in response to an auditory cue, STN-projecting neurons in the deep layer of the prefrontal areas were preferentially active in no-go trials, and the tendency to initiate motor responses could be manipulated by the neurons (30, 31). M2-STN projections appear to play a role in both stopping and planning to stop locomotive activity (32). Supporting this idea, optogenetic stimulation of M2 axons modulated the locomotor activity in healthy and dopamine-depleted mice (33). However, while the effect of DBS-STN on the primary motor cortex (M1) has become clearer (34–39), it remains relatively unknown if and how high-frequency antidromic activation of M2 may be involved.

Hyperpolarization-activated cyclic-nucleotide gated (HCN) channels, the cation channels activated upon hyperpolarization, exhibit dichotomous effects on circuit activity regulation. On one hand, HCN channels contribute to the depolarization of the resting membrane potential as HCN channels are active under -50 mV, thereby promoting action potential generation (40). Furthermore, hyperpolarization-induced rebound depolarization triggers subsequent action potentials in certain neurons (41–43). Conversely, channel conductance in resting neurons reduces input resistance, leading to decreased integration and regenerative activity of dendrites (44, 45). In addition to modulating neuronal excitability, HCN channels have been implicated in synchronizing neural networks to theta-frequency oscillation (46–50). Notably, decreased HCN conductance correlated with reduced theta resonance in rodents (51). However, despite the

importance of the channels in the regulation of neuronal excitability and network oscillation, the involvement of cortical HCN channels in PD remains less understood.

In this study, we aimed to investigate the potential role of antidromic M2 stimulation during STN-DBS in alleviating motor symptoms in a PD mouse model.

## Results

*Characterization of M2 circuits and behavior in the PD mouse model with medial forebrain lesions with 6-hydroxydopamine (6-OHDA)*

The PD mouse model was established by the unilateral stereotaxic administration of 6-OHDA into the medial forebrain bundle (MFB). As expected, we found a substantial reduction in the density of tyrosine hydroxylase (TH)-expressing neurons in the caudoputamen and substantia nigra pars compacta compared with that in the intact hemisphere (Fig. S1A). It was evident that the PD model mice exhibited abnormalities in movement. To attain the behavioral validation of the mouse model, we used a hanging wire test to assess suspension time as mice tried to avoid falling (52–54). The hanging time of control mice increased as the test was repeated, perhaps by learning the motor coordination required for hanging. Contrastingly, 6-OHDA-lesioned mice showed a decrease in hanging time (Fig. S1B). We also analyzed the gait pattern of the PD model mice as they walked on a treadmill at a speed of 17 cm/s (Fig. S1C-D). The stance, stride time, and stride length on the contralateral side of the damaged hemisphere were significantly reduced (Fig. S1E). Contrastingly, the stride frequency increased, perhaps to keep up with the speed of the treadmill. The paw area touching the ground varied significantly more than that of control mice, suggesting a less standardized walking pattern.

Having established the PD mouse model, we examined the basal firing rate of the M2 neurons in a PD mouse model by analyzing the single-unit activity (Figure 1A-B). Consistent with the idea that enhanced M2 neuron activity is involved in the motor-stopping activity in PD symptoms, well-isolated single units demonstrated significantly higher firing frequencies with a greater likelihood of burst firing in the M2 of the PD model (Fig. 1D and E).

Previous studies revealed that fronto-subthalamic inhibitory motor control is mediated by beta-frequency oscillation in humans (23, 24), and enhanced synchrony in the beta-frequency range is correlated with bradykinesia in PD patients (55). To test if the enhanced M2 activity is represented in the form of oscillatory synchronous neural activity, we analyzed the local field potential (LFP) in the M2 of the PD mouse model. We found a significant increase in synchronous oscillatory activities over a wide frequency range, with the most dramatic increase in the theta frequency range (Figure S2). These results supported our hypothesis that the enhanced motor-stopping signal, originating from the M2 through a hyperdirect pathway, may contribute to dyskinesia in a PD mouse model.

We then examined whether increased M2 activity can be explained by M2 neuronal membrane property changes in acutely prepared brain slices of PD mouse models (Figure 1F-M). In corroboration with the increased burst firing and network oscillations (41–43), we found the maximum firing frequency by depolarizing current injection was greater in the PD mouse model. Also, the hyperpolarization-activated cation current ($I_h$), measured by the amplitude of voltage sag by -200 mV current injection, was significantly enhanced (Figure 1M). The enhanced excitability in M2 was further established by the enhanced frequency of spontaneously evoked postsynaptic

current (sEPSCs) (Fig. S3). Our results suggest that M2 basal activity is significantly enhanced in the PD mouse model.

*Electrical STN stimulation antidromically excites M2 neurons*

To test if M2 neuronal activity is involved in the effect of DBS-STN, we first verified the direct synaptic connections between M2 neurons and the STN. We delivered retrograde adeno-associated virus (rAAV2-retro) to the STN of the transgenic mouse line that expresses channelrhodopsin-2 (ChR2) conjugated with tdTomato in a cyclic recombinase (Cre)-dependent manner (Rosa-CAG-LSL-hChR2[H134R]-tdTomato-WPR or Ai27D) (Fig. 2A-B) (56, 57). As previously described (30–33), we found that a considerable portion of the layer (L) 5 M2 neurons was retrogradely labeled, suggesting direct synaptic connections to the STN (Fig. 2B). Furthermore, we observed a prompt increase in multiunit activity in M2 neurons upon electrical stimulation, imitating DBS-STN (Fig. 2C-D). These results suggest the modulation of M2 neuron activity by DBS-STN and its possible involvement in the effects of DBS-STN.

*High-frequency stimulation of STN-projecting M2 neurons and the impact on network synchrony and behavioral abnormalities in the PD mouse model*

If antidromic stimulation of M2 is involved in the DBS-STN mechanism, the stimulation of STN-projecting M2 neurons should mimic the effect of DBS-STN to a certain extent. To test this, we analyzed animal behavior upon optogenetic stimulation of STN-projecting M2 neurons (Fig. 3). Given the relevance of the theta power to forelimb strength and stride pattern associated with gait freezing and voluntary gripping in PD patients (58, 59), we conducted wire-hanging tests and gait analysis. The observed abnormalities in forelimb strength and stride pattern (Fig. S1) significantly improved immediately after optogenetic stimulation of STN-projecting M2 neurons (Fig. 3, 473 nm, 9 mW/mm$^2$, 2 msec square pulses at 140 Hz, 3 min). We found that the latency of falling from the wire significantly increased in response to optogenetic stimulation (Fig. 3B). Likewise, the gait pattern of 6-OHDA-lesioned mice was remarkably normalized (Fig. 3C-E). Specifically, optogenetic stimulation increased propulsion, stance, stride time, stride length, stride frequency, and variability of the paw area.

Thus far, our results suggested that M2 neurons in the PD model were hyperexcited with increased oscillatory synchrony, and high-frequency stimulation of STN-projecting M2 neurons ameliorated PD model behavioral abnormalities in a similar way with DBS-STN (36, 60). We then examined whether the improvement in behavioral abnormalities was associated with electrophysiological normalization. Indeed, optogenetic stimulation of STN-projecting M2 neurons significantly reduced oscillatory synchrony (Fig. S4). Particularly, a reduction in oscillatory synchrony was observed in the theta frequency range (Fig. S4G). Furthermore, optogenetic stimulation modulated the frequency of well-isolated single units recorded in the M2 (Fig. 4). Although frequency modulation varied widely, stimulation reduced the firing frequencies and burst firing duration of the M2 units in the population, with significant effects lasting several minutes after the stimuli ended (Fig. 4C-E).

To further examine whether baseline activity may explain the direction of modulation, we grouped units depending on frequency modulation direction (Fig. 4F, black and red plots). The units whose frequency was decreased by optogenetic stimulation had significantly higher baseline activity. However, units with moderate baseline activity showed no changes or a slight increase in activity. Also, the magnitude of firing frequency reduction by the stimulation correlated with pre-stimuli baseline activity (Fig. 4G). The two groups of units had comparable kinetic properties, suggesting that STN-projecting M2 neurons are mostly regular spiking neurons (Fig. S5). Thus, our findings

suggested that optogenetic stimulation of STN-projecting M2 neurons relieved the hyperactivity of the M2 circuit, and that modulation efficacy may differ depending on baseline activity levels.

*The impact of the high-frequency electrical STN stimulation on M2 neuron activity*

The effect of optogenetic stimulation of STN-projecting M2 neurons may differ from antidromic M2 activation during electrical STN stimulation, considering factors such as fidelity of antidromic stimulation, difference in action potential kinetics, and synaptic transmission (61, 62). To directly address this potential difference, we examined whether the amelioration of M2 hyperactivity may be replicated by electrical STN stimulation (Fig. 5). The stimulation electrode was placed in the electrophysiologically identified STN, while the activity of M2 neurons was monitored extracellularly before, during, and after stimulation. In line with the optogenetic stimulation findings, isolated M2 unit frequencies were significantly reduced by electrical stimulation (Fig. 5C). Contrastingly, the M2 neuron frequencies showed the opposite effect in control mice (Fig. 5D), suggesting that the M2 frequency reduction is specific to PD-like symptoms.

*M2 neural excitability upon optogenetic M2 stimulation*

To explore the cause of the reduced M2 neurons firing, we analyzed the membrane properties of M2 neurons of 6-OHDA-lesioned mice upon optogenetic stimulation *ex vivo*. Approximately four weeks after the MFB lesion, when the behavioral symptoms became noticeable, we measured M2 neuronal excitability before and after optogenetic stimulation with whole-cell recordings. Corroborating our *in vivo* observations, we found a significant reduction in excitability by optogenetic stimulation of STN-projecting M2 neurons. Significantly fewer action potentials were evoked in response to depolarizing current injections at all amplitudes examined (Fig. 6A-C). Despite a slightly depolarized resting membrane potential (Fig. 6C) and a comparable threshold (Fig. 6D), a significantly larger depolarizing current was required to evoke an action potential (Rheobase, Fig. 6E). We attributed this reduced excitability to the reduced input resistance (Fig. 6F) and hyperpolarization-evoked depolarizing voltage sag (Fig. 6G).

Previously, it has been shown that, during DBS-STN stimulation, antidromically stimulated M1 neurons temporally suppressed M1 circuits via somatostatin-expressing inhibitory (SST) neuron activation (39). To examine whether similar circuit suppression may be involved in the M2, we examined spontaneously evoked excitatory and inhibitory synaptic currents (sEPSC and sIPSC, respectively). If similar circuit suppression was involved, enhanced sIPSC frequency and reduced sEPSC could be expected. However, we did not find any significant alterations in spontaneous synaptic frequencies (Fig. S6), suggesting that the reduced excitability of M2 neurons is unlikely to be mediated by the same circuit mechanism as the M1.

*HCN channel dependency of high-frequency M2 stimulation-induced behavioral amelioration*

Considering the increased burst firing and theta-band oscillation observed in the Parkinson's disease (PD) model, along with their reversal through STN stimulation, we investigated whether concurrent changes in the $I_h$ current could account for these alterations in neural activity and behavioral improvement (41–43). To examine the behavioral impact of reduced HCN channel activity in M2, we administered ZD7288, a selective HCN channel blocker, into the M2 region of PD mice, and subsequently assessed the effects on behavioral abnormalities (Fig. 7A). Remarkably, we observed a significant improvement in behavioral abnormalities, as evidenced by enhancements in wire-hanging time and gait patterns (Fig. 7). These findings strongly suggest

that the observed behavioral improvement upon M2 neuron stimulation can be attributed to reduced HCN channel activity.

## Discussion

In this study, we explored the possibility that repetitive antidromic activation of M2 neurons during DBS-STN may be involved in the effects of DBS. We hypothesized that hyperexcitability and normalization of the STN and its upstream premotor areas, which are associated with motion-stopping (3, 4, 22–25, 31, 32, 63), contribute to the motor dysfunction observed in PD, while the normalization of these areas through DBS-STN alleviates motor symptoms. In line with previous reports (30–33), we found that a notable population of L5 neurons in M2 project directly to the STN in mice and are activated by electrical stimulation of the STN (Fig. 2), illustrating the possible involvement of M2 neurons during DBS-STN. To isolate the effect of high-frequency activity during DBS-STN, we used optogenetic stimulation of STN-projecting M2 neurons (Fig. 3A). High-frequency stimulation of these neurons mimicking DBS alleviated the behavioral (Fig. 3) and synchronized oscillatory abnormalities (Fig. S4) observed in the PD mouse model. The causality of network oscillations with motor impairment was not directly addressed in this study. However, oscillatory activity has been observed to be repeatedly correlated with the level of motor impairment in both patients with PD and animal models (64, 65). Furthermore, the premotor areas directly connected to the STN have been indicated as the source of oscillation during stop-signal responses (23, 66). Thus, we hypothesized that the hyperexcitability of STN-projecting M2 neurons could be a source of dyskinesia in PD.

Consistent with our hypothesis, we found that the STN-projecting M2 neurons can fire at significantly higher frequencies in the PD model than in the sham-control mice (Fig. 1), which can be suppressed upon optogenetic stimulation accompanied by behavioral amelioration (Fig. 3 and 4). The reduced activity of M2 neurons upon optogenetic stimulation could be recapitulated *ex vivo*, where we found a significant reduction in the firing frequency in response to the depolarizing current injection (Fig. 6). This phenomenon could be attributed to the reduced $R_{in}$, which requires greater excitatory inputs to fire an action potential. Moreover, diminished $I_h$ current, the hallmark of the HCN channel, could contribute to reducing the repetitive firing of neurons (43, 67, 68). Consequently, our results demonstrated that the reduced HCN channels in M2 mimicked the effects of DBS-STN to some extent (Fig. 7).

*Oscillatory network activity in the M2*

Typically, enhanced beta-frequency oscillations are reported to correlate with movement abnormalities in the STN of patients with PD (55). However, in studies using various animal models, the increase in beta frequency was not consistent. Instead, synchronous oscillations in lower-frequency ranges, such as theta, were observed (69–74). Similarly, enhanced oscillatory power in the lower-frequency range, including the theta band, was observed in some studies of patients with PD (58, 59, 75–77). Thus, it is feasible that enhanced synchronous neural activity itself is the pathological hallmark of PD, whereas the abnormal frequency range is related to the type of motor symptoms (59, 73). Increased synchrony in the theta range in the STN and pre-SMA was correlated with gait freezing and hand use (11, 58, 59, 78). Correspondingly, we observed gait abnormalities and shortening of the hanging time, along with the power of oscillation in all frequency ranges, the greatest being in the theta range (Fig.S2 and 3). Furthermore, we found that selective stimulation of STN-projecting M2 neurons significantly reduced the theta frequency range, together with the behavioral symptoms, of PD mice (Fig. S4 and 3). The observed enhancement of oscillatory synchronization in the M2 region of the PD mouse model, as well as its normalization through M2 stimulation, corresponded to concurrent changes in $I_h$ current (Fig. 1 and 6). Distally enriched distribution and inductance by HCN channels synchronize the distal and somatic voltage waveform, with maximum synchronization occurring within the theta frequency range (47–50). While previous studies have primarily

investigated hippocampal pyramidal neurons, similarly polarized HCN distribution in neocortical pyramidal neurons suggests a potential for a similar synchronization effect (79, 80).

*Antidromic STN-projecting neurons during DBS-STN*

The activity of STN neurons is dependent on many brain areas in addition to the M2. Notably, M1 involvement has attracted considerable attention. High-frequency optogenetic stimulation of M1 neurons, or afferent axons from the M1, improved the behavior efficiently (34, 38). A recently published study showed that DBS-STN relieves the M1 circuits from overexcitation by activating SST-expressing inhibitory neurons in the M1 (39). We tested whether a parallel phenomenon occurs in the M2 by measuring the frequencies of sEPSCs and sIPSCs. We could not detect any significant frequency changes after high-frequency stimulation of the STN-projecting M2 neurons (Fig. S6). However, we cannot rule out local inhibitory neuronal involvement in normalized M2 activity if the effect of the inhibitory neuron lasts only during stimulation. In fact, the enhanced activity of SST neurons in the M1 lasted less than a minute (39), which may not be long enough to reliably detect frequency changes in sIPSCs. It is unlikely that the effect of GABAergic synaptic transmission activated by STN-projecting neurons lasts longer than that time scale. It is noteworthy that all behavioral and electrophysiological changes illustrated in our study were measured after stimulation of STN-projecting M2 neurons. Furthermore, feedforward inhibition-mediated circuit silencing is difficult to reconcile with the selectivity effect observed in the M2. We observed that optogenetic stimulation occurred selectively in the set of units with high baseline activity, but not in neurons with low baseline activity or in control mice (Fig. 4 F-G and Fig. 5). Together, we propose that excitability reduction, not inhibitory neuron-mediated suppression, is the leading cause of the long-lasting effects of DBS-STN. The observed effect of M2 stimulation in this study was not mutually exclusive from previous studies that implicated the involvement of M1 in the therapeutic effect of DBS-STN. In fact, we believe that the therapeutic effect of DBS-STN could be due to a combination of various circuit modulations, including the M1 and M2, each of which may relate to different effect times and behavioral symptoms.

*Study novelty*

Similar to this study, Magno et al. (33) found that high-frequency M2 stimulation alleviates behavioral PD-like symptoms in 6-OHDA mice. However, they accounted for this phenomenon via the striatum's increased dopamine concentration. We did not directly measure dopamine replenishment in our study. However, we found no changes in the aperiodic components of the subthalamic LFP (Fig. S7), which have been reported to vary with striatal dopamine concentration (81). This result suggests that dopamine may not be the primary explanation for the optogenetic M2 stimulation under our experimental conditions. This apparent discrepancy can be explained by differences in the population of stimulated M2 neurons. Magno et al. transduced ChR2 into excitatory neurons in all layers of the M2 and stimulated M2 or M2 axons passing the dorsomedial striatum (33). Thus, optogenetic stimulation could have influenced wide brain areas, including the ventral tegmental area, the major source of dopaminergic neurons. In this study, we selectively stimulated STN-projecting M2 neurons to study M2 circuit modulation. Therefore, this study directly addressed the therapeutic contribution of antidromic M2 stimulation to DBS-STN.

*Limitations of the study*

While M2 activity modulation has therapeutic potential, several essential issues remain. First, future research should determine whether the reduced activity or decreased excitability is sufficient to ameliorate PD-like symptoms of the mouse model. Furthermore, it remained unclear how dopamine depletion causes hyperexcitability in the M2 region of the PD mouse model. The optimal activation frequency of the STN-projecting M2 neurons needed to achieve the therapeutic effects remained unclear in this study. Although we observed improved behavioral and electrophysiological symptoms using 140-Hz optogenetic stimulation, the actual firing frequency and duration of the STN-projecting M2 neurons could not be determined because of the low fidelity action potentials by high-frequency ChR2 stimulation. Likewise, while we observed a reduced firing rate of the M2 neurons by antidromic electrical stimulation with the same frequency

at the STN, somatic firing frequency should be significantly lowered by voltage filtering through axons (61, 62). Thus, a systematic comparison with different stimulation frequencies may be required.

*Significance and future perspectives*
Our study has important implications and opens new avenues for future research. First, our findings provide a scientific basis for the development of less invasive approaches for stimulating the frontal cortices that project to the subthalamic nucleus (STN), while still preserving the therapeutic effects of deep brain stimulation of the STN (DBS-STN) (24–26). This could potentially lead to the development of novel stimulation techniques that are more targeted and have fewer side effects.

Furthermore, our study highlights the potential of targeting excessive activity in the M2 region as a therapeutic strategy for alleviating motor symptoms in Parkinson's disease (PD). The significant improvement in motor abnormalities observed with HCN channel blockers in our PD mouse model suggests that these channels could serve as promising drug targets for PD treatment. Further exploration of HCN channel blockers and their effects on PD symptoms in clinical settings is warranted.

Overall, our findings shed light on the mechanisms underlying the therapeutic effects of DBS-STN and present new opportunities for the development of less invasive stimulation techniques and potential drug therapies for PD. Further investigations into these areas hold great promise for improving the quality of life for individuals living with PD and advancing our understanding of the neural circuits involved in motor control.

**Materials and Methods**

*Animals*
Transgenic mice expressing the ChR2 variant, ChR2 H134R, fused to tdTomato were generated by crossing heterozygous B6.Cg-Gt(ROSA)$^{26Sortm\ 27.1(CAG\text{-}COP4*H134R/tdTomato)Hze}$/J (Ai27D; Jackson Laboratory, Bar Harbor, ME, USA; stock number 012567) and C57BL/6J (Jackson Laboratory, Bar Harbor, ME, USA; stock number 000664) mice. Mice were placed in a 12 h reversed light/dark cycle (lights on at 8 p.m.) with ad libitum access to standard chow and water. All animal experiments were approved by the Institutional Animal Care and Use Committee of the Korea Brain Research Institute (IACUC 22-00009).

*Stereotactic surgery*
A total of 81 male mice were randomly assigned to the following two groups: 6-OHDA lesioned mice (n = 66) and control mice (n = 15). Mice were anesthetized with a ketamine-xylazine mixture of 100 mg/kg ketamine-10 mg/kg xylazine and positioned in a stereotaxic apparatus (RWD Life Science Inc., San Diego, CA, USA). Body temperature was controlled throughout the procedure using a feedback heating pad. Thirty minutes prior to intrastriatal injection, mice received desipramine (10 mg/kg intraperitoneal injection [i.p.], Sigma, St. Louis, MO, USA) to protect noradrenergic terminals against 6-OHDA-induced damage.

We injected 6-OHDA hydrochloride (Sigma, St. Louis, MO, USA) to unilaterally lesioned dopamine neurons (using a 10 μL NanoFil syringe [WPI, Sarasota, FL, USA] connected to an automated pump at 80 nL/min [UltraMicroPump and SYS-Micro4 Controller, WPI, Sarasota, FL, USA]) in the MFB [anteroposterior (AP): -1.1 mm; mediolateral (ML): -1.1 mm; dorsoventral (DV): -4.7 mm; coordinates from Paxinos and Franklin, 2001 (80)] of middle-aged adult mice (10-12 weeks). The 6-OHDA animals were injected with 300 nL of 6-OHDA hydrochloride (5 μg/μL) with 0.2 mg/mL ascorbic acid in 0.9% NaCl, while the control animals received the same volume of

vehicle solution at the same coordinates. This method produced strong nigrostriatal lesioning, as verified histologically through TH staining.

In the same surgery, adeno-associated viruses carrying a retrograde tracer, Cre construct (Ef1a-mCherryIRES-WGA-Cre), were injected in the STN (AP: -1.8 mm; ML: -1.56 mm; DV: −4.3 mm from the bregma). Chronic optical fiber implants were manufactured in ceramic ferrules with 200 μm inner diameter (RWD Life Science Inc., San Diego, CA, USA) in the M2 (AP:1.7 mm; ML: -0.6 mm). Ketoprofen (5 mg/kg) was injected subcutaneously once daily for three days. Mice were allowed to recover for 4 weeks after virus injection to allow axonal expression of opsin.

For experiments, HCN channel blocker microinjection, a stainless-steel guide cannula (26-gauge stainless steel wire, Plastics One, Roanoke, VA) was implanted into the M2 (AP:1.7 mm; ML: -0.6 mm), and a dummy cannula (33-gauge stainless steel wire, Plastics One, Roanoke, VA) was inserted into the guide cannula to reduce the incidence of occlusion. The guide cannula was fixed to the skull using a super-bond. HCN channel blocker, ZD7288 (Tocris, Bristol, UK) solutions was infused into the M2 using a microinjection unit (33-gauge cannula) that attached to a 10 μL NanoFil syringe via polyethylene tubing (PE-50). ZD7288 was dissolved in sterile saline and infused into the M2 (300nl, 80 nl / min).

*Electrophysiology*

*In-vivo recording*

For *in-vivo* electrophysiological experiments, mice were anesthetized with ketamine (100 mg/kg, i.p.) and placed in a stereotaxic device (WPI, Sarasota, FL, USA). In all surgical preparations, the scalp was incised and holes were drilled in the skull overlying the site of recording or stimulation, according to the coordinates from the atlas of Paxinos and Franklin (80): M2: AP: +1.7 mm from the bregma, ML: ± 0.6 mm from the midline, and DV: -0.5-0.7 mm below the dura; STN: AP: -4.3 mm from the bregma, ML: 1.56 mm from the midline at an anteroposterior angle of 30°, and DV: -4.8-5.0 mm below the dura. An additional hole was drilled over the other cortex in the left hemisphere to implant a microscrew that was used as a recording reference. During the recording, the brain surface was kept wet by dropwise addition of saline.

To record M2 responses, 16-channel silicon electrodes with a fiber optic ferrule (200 μm diameter, A1×16-5mm-100-177-OA16LP; NeuroNexus, Ann Arbor, MI, USA) were used. The optoelectrode was gradually lowered until the tip was positioned at a depth of ~700 μm under the surface. Light stimulation was provided by a 473 nm laser with a laser power set to 9 mW, as measured at the tip of the fiber (0.22 NA; Doric Lenses, Quebec, Canada), to be connected to the ferrule on the mouse's head. Neuronal activity was amplified and digitized using a PZ5 NeuroDigitizer and RZ5D BioAmp Processor (TDT, Alachua, FL, USA) with a 24,414 Hz/channel sampling rate and bandpass filtered between 0.3 and 5 kHz. Single units were identified and sorted into clusters by Opensorter (TDT, Alachua, FL, USA) and further analyzed using NeuroExplorer (NEX Technology, Colorado Springs, CO, USA). Viral expression was allowed for a minimum of 4 weeks before behavioral testing.

Four-limb hanging-wire test

The four-limb hanging-wire test was performed to examine motor function impairments. Each mouse was placed on the wire lid of a conventional housing cage, which was then turned upside down. The time spent hanging was recorded from the time of inversion until all paws were released from the grid.

Automated treadmill gait test

Gait analysis was performed using DigiGait software and a treadmill (Mouse Specifics, Inc., Framingham, MA, USA) from 5 weeks after administration of 6-OHDA. Mice were placed on a

motorized treadmill within a plexiglass compartment (~25 cm long and ~5 cm wide). Digital video recordings were acquired using a camera mounted underneath the treadmill to visualize paw contacts on the treadmill belt. The treadmill was set at a fixed speed of 17 cm/s, at which most animals were able to move continuously. Mice were allowed to accommodate the movement of the treadmill for several seconds before the gait analysis. The gaits during the first 5 s after the acclimation period were analyzed using DigiGait software, which automatically identifies paw footprints and processes them to calculate values for multiple gait parameters, including stride frequency and length, paw area CV, and paw angle (Figure S1).

*Euthanasia*
Mice were deeply anesthetized with ketamine (100 mg/kg, i.p.) and transcardially perfused with ice-cold dissection solution or 4% paraformaldehyde in 0.01 M phosphate-buffered saline (PBS). The brains were removed for histological or electrophysiological studies.

*Ex-vivo* whole-cell recording
To prepare *ex-vivo* slices for whole-cell recording, brains were removed and immersed in an ice-cold cutting solution with the following composition (in mM): choline chloride, 110; KCl, 2.5; $NaHCO_3$, 25; $NaH_2PO_4$, 1.25; glucose, 25; $CaCl_2$, 0.5; $MgCl_2 \cdot 6H_2O$, 7; sodium ascorbic acid, 11.6; and pyruvic acid, 3. The measured osmotic concentration was 320–330 mOsm.

We prepared 300 µm thick acute brain slices containing M2 coronally using a VT1200S Vibratome (Leica Biosystems, Deer Park, IL, USA). The composition of artificial cerebrospinal fluid (aCSF) was (in mM): NaCl, 119; KCl, 2.5; $NaHCO_3$, 26; $NaH_2PO_4$, 1.25; glucose, 20; $CaCl_2$, 2; $MgSO_4$, 1; ascorbic acid, 0.4; and pyruvic acid, 2. The osmotic concentration was 305–310 mOsm.

During sectioning, the solutions were oxygenated using 95% $O_2$ and 5% $CO_2$. After 30 min of recovery time at 32 °C, aCSF slices were transferred to room temperature. Recordings were performed using patch pipettes (3.5–5 MΩ) filled with an internal solution consisting of the following (in mM): KCl, 20; potassium gluconate, 125; HEPES, 10; NaCl, 4; EGTA, 0.5; ATP, 4; TrisGTP, 0.3; and phosphocreatine, 10 (pH 7.2, 290–300 mOsm).

Immunohistochemistry
Brains were removed and post-fixed for 12 h at 4 °C. Coronal sections (50 µm) were obtained using a vibratome (VT1000S; Leica, Nussloch, Germany). Slices were immersed in 0.2% Triton X-100 Tris-buffered saline solution (TBS-T) for 10 min, followed by blocking for 1 h with 0.2% Triton X-100 and 5% normal goat serum (Jackson ImmunoResearch, Suffolk, UK) in PBS. Sections were washed in TBS-T and incubated overnight at 4 °C in the same buffer with anti-TH monoclonal antibodies (1:500; Millipore, Stockholm, Sweden). Immunoreactivity was detected using a secondary antibody conjugated with Alexa fluorescent dye (1:400; Jackson Laboratory, Bar Harbor, ME, USA) for 3 h at room temperature. The slices were mounted on glass slides with a mounting solution containing DAPI (4',6-diamidino-2-phenylindole; Vectashield with DAPI, Vector Laboratories, Burlingame, CA, USA). Images were acquired using a slide scanning system (Panoramic Scan, 3DHistech, Ltd., Budapest, Hungary).

*Statistical Analysis*
Data acquisition and analysis with commercial systems
Data acquisition and analysis were performed using TDT processors and Opensorter (TDT, Alachua, FL, USA), Synapse Software (Synapse Software, Colorado Springs, CO, USA), and NeuroExplorer (NEX Technology, Colorado Springs, CO, USA). MATLAB (MathWorks, Natick, MA, USA) and GraphPad Prism 6.0 (GraphPad Software, San Diego, CA, USA) were used for further statistical analyses. All data are presented as mean ± standard error, unless otherwise indicated. Statistical comparisons of two variables from an identical set of subjects were

performed using paired *t*-tests. Otherwise, an unpaired *t*-test or Mann–Whitney U test was used. Statistical significance was defined as p-values < 0.05, <0.01, and <0.001, as indicated.

Stimulation artifact removal using the Period-based Artifact Reconstruction and Removal Method (PARRM) algorithm
As we used a threshold-based spike-sorting algorithm, we sought to remove artifacts caused by stimulation. We adopted the PARRM algorithm: the latest stimulation artifact removal method requiring only a few hyperparameters to be tuned (81). We adjusted the parameters (stimRate = 140, fs = 24,414, winSize = 10·fs, skipSize = floor(fs·0.01), winDir = “both”, and perDist = 0.1) and applied the algorithm to the data for the stimulation period only.

Spike-sorting using the wave_clus algorithm
For the stimulation artifact removed data, we sorted single units with the wave_clus algorithm, an automatic spike-sorting algorithm based on wavelet coefficients (82). We adjusted the parameters as follows: sr = 24,414, w_pre = 20, w_post = 44, alignment_window = 20, detection = “neg”. After the automatic sorting procedure, we manually merged and split the clusters based on the feature space extracted using the algorithm.

Parameterization of the aperiodic component in LFP using the SpecParam algorithm
To parameterize the aperiodic component of LFP, we used the SpecParam algorithm, also known as Fitting Oscillations and One-Over-f (FOOOF) (83). Before using the SpecParam algorithm, we linearly interpolated the neural power spectral densities at approximately 60 Hz in the log-log space (i.e., the logarithm of frequency and power) to relieve the notch filter effects. We adjusted the parameters (max_n_peaks = 4, min_peak_height = 0.15, peak_width_limts = [1; 20], and aperiodic_mode = “fixed”) and used the input frequency range of 6–110 Hz to avoid oscillations crossing the fitting range borders (84). Note, here we used the “fixed” mode (i.e., the knee parameter k=0), because the “knee” mode generated worse fits for several data sets than the “fixed” mode.

**Acknowledgments**

**Funding:**
Korea Brain Research Institute Research Programs, grant 23-BR-01-01, 23-BR-03-01, and 23-BR-04-04 (JCR).
National Research Foundation of Korea, funded by the Ministry of Science and Information and Communication Technology, grant NRF-2017M3A9G8084463 and NRF-2022R1A2C1004216 (JCR).
Korea Research Institute of Bioscience and Biotechnology (KRIBB) Research Initiative Program (KGM5282322) (JCR).

We thank Drs. John Isaac, Jaewon Ko, and Jinhyun Kim for their helpful comments. Schematic diagrams were adapted from reset images of BioRender.com, and grammatical errors were corrected by ChatGTP and Elsevier Language Editing Service.

**Author contributions:**
Study design: J-CR, ISC
Data gathering and analysis: ISC
Further analysis of the *in-vivo* electrophysiology data: JMK
Project supervision: J-CR, JWC
Writing: All authors contributed

**Competing interests:** Authors declare that they have no competing interests.

**Data and materials availability:** All data are available at https://doi.org/10.6084/m9.figshare.6025748.v1

**References**


1. A. R. Aron, R. A. Poldrack, Cortical and subcortical contributions to stop signal response inhibition: role of the subthalamic nucleus. *J. Neurosci.* 26, 2424–2433 (2006).

2. R. Schmidt, D. K. Leventhal, N. Mallet, F. Chen, J. D. Berke, Canceling actions involves a race between basal ganglia pathways. *Nat. Neurosci.* 16, 1118–1124 (2013).

3. A. Emmi, A. Antonini, V. Macchi, A. Porzionato, R. De Caro, Anatomy and connectivity of the subthalamic nucleus in humans and non-human primates. *Front. Neuroanat.* 14, 13 (2020).

4. D. M. Eagle, *et al.*, Stop-signal reaction-time task performance: Role of prefrontal cortex and subthalamic nucleus. *Cereb. Cortex* 18, 178–188 (2008).

5. K. H. Fife, *et al.*, Causal role for the subthalamic nucleus in interrupting behavior. *Elife* 6 (2017).

6. I. Hamada, M. R. DeLong, Excitotoxic acid lesions of the primate subthalamic nucleus result in transient dyskinesias of the contralateral limbs. *J. Neurophysiol.* 68, 1850–1858 (1992).

7. T. Z. Aziz, D. Peggs, M. A. Sambrook, A. R. Crossman, Lesion of the subthalamic nucleus for the alleviation of 1-methyl-4-phenyl-1,2,3,6-tetrahydropyridine (MPTP)-induced parkinsonism in the primate. *Mov. Disord.* 6, 288–292 (1991).

8. H. Bergman, T. Wichmann, M. R. DeLong, Reversal of Experimental Parkinsonism by Lesions of the Subthalamic Nucleus. *Science.* 249, 1436–1438 (1990).

9. J. R. Whittier, F. A. Mettler, Studies on the subthalamus of the rhesus monkey. II. Hyperkinesia and other physiologic effects of subthalamic lesions, with special reference to the subthalamic nucleus of Luys. *J. Comp. Neurol.* 90, 319–372 (1949).

10. H. Bergman, T. Wichmann, B. Karmon, M. R. DeLong, The primate subthalamic nucleus. II. Neuronal activity in the MPTP model of parkinsonism. *J.Neurophysiol.* 72, 507–520 (1994).

11. S. Breit, *et al.*, Effects of 6-hydroxydopamine-induced severe or partial lesion of the nigrostriatal pathway on the neuronal activity of pallido-subthalamic network in the rat. *Exp. Neurol.* 205, 36–47 (2007).

12. O. K. Hassani, M. Mouroux, J. Féger, Increased subthalamic neuronal activity after nigral dopaminergic lesion independent of disinhibition via the globus pallidus. *Neuroscience* 72, 105–115 (1996).

13. P. J. Magill, J. P. Bolam, M. D. Bevan, Relationship of activity in the subthalamic nucleus–globus pallidus network to cortical electroencephalogram. *J. Neurosci.* 20, 820–833 (2000).

14. M. S. Remple, *et al.*, Subthalamic nucleus neuronal firing rate increases with Parkinson's disease progression. *Mov. Disord.* 26, 1657–1662 (2011).

15. A. M. Lozano, *et al.*, Deep brain stimulation: current challenges and future directions. 15, 148–160 (2019).

16. E. B. Montgomery, K. B. Baker, Mechanisms of deep brain stimulation and future technical developments. *Neurol. Res.* 22, 259–266 (2000).

17. N. Schweizer, *et al.*, Limiting glutamate transmission in a Vglut2-expressing subpopulation of the subthalamic nucleus is sufficient to cause hyperlocomotion. *Proc. Natl. Acad. Sci. U. S. A.* 111, 7837–7842 (2014).

18. A. R. Aron, P. C. Fletcher, E. T. Bullmore, B. J. Sahakian, T. W. Robbins, Stop-signal inhibition disrupted by damage to right inferior frontal gyrus in humans. *Nat. Neurosci. 2003 62* 6, 115–116 (2003).

19. K. Rubia, A. B. Smith, M. J. Brammer, E. Taylor, Right inferior prefrontal cortex mediates response inhibition while mesial prefrontal cortex is responsible for error detection. *Neuroimage* 20, 351–358 (2003).

20. C.-S. R. Li, C. Huang, R. T. Constable, R. Sinha, Imaging response inhibition in a stop-signal task: neural correlates independent of signal monitoring and post-response processing. *J. Neurosci.* 26, 186–192 (2006).

21. P. Nachev, H. Wydell, K. O'Neill, M. Husain, C. Kennard, The role of the pre-supplementary motor area in the control of action. *Neuroimage* 36, T155–T163 (2007).

22. N. C. Swann, *et al.*, Roles for the pre-supplementary motor area and the right inferior frontal gyrus in stopping action: Electrophysiological responses and functional and structural connectivity. *Neuroimage* 59, 2860–2870 (2012).

23. M. Schaum, *et al.*, Right inferior frontal gyrus implements motor inhibitory control via beta-band oscillations in humans. *Elife* 10 (2021).

24. K. K. Sundby, S. Jana, A. R. Aron, Double-blind disruption of right inferior frontal cortex with TMS reduces right frontal beta power for action stopping. *J. Neurophysiol.* 125, 140–153 (2021).

25. T. M. Mi, *et al.*, High-frequency rTMS over the supplementary motor area improves freezing of gait in Parkinson's disease: a randomized controlled trial. *Parkinsonism Relat. Disord.* 68, 85–90 (2019).

26. T. M. Mi, *et al.*, Repetitive transcranial magnetic stimulation improves Parkinson's freezing of gait via normalizing brain connectivity. *npj Park. Dis. 2020 61* 6, 1–9 (2020).

27. A. R. Aron, T. E. Behrens, S. Smith, M. J. Frank, R. A. Poldrack, Triangulating a cognitive control network using diffusion-weighted magnetic resonance imaging (MRI) and functional MRI. *J. Neurosci.* 27, 3743–3752 (2007).

28. B. U. Forstmann, *et al.*, Cortico-striatal connections predict control over speed and accuracy in perceptual decision making. *Proc. Natl. Acad. Sci. U. S. A.* 107, 15916–15920 (2010).

29. F. Barthas, A. C. Kwan, Secondary motor cortex: where ‘sensory’ meets ‘motor’ in the rodent frontal cortex. *Trends Neurosci.* 40, 181–193 (2017).

30. T. Kamigaki, Y. Dan, Delay activity of specific prefrontal interneuron subtypes modulates memory-guided behavior. *Nat. Neurosci.* 20, 854–863 (2017).

31. B. Li, T. P. Nguyen, C. Ma, Y. Dan, Inhibition of impulsive action by projection-defined prefrontal pyramidal neurons. *Proc. Natl. Acad. Sci. U. S. A.* 117, 17278–17287 (2020).

32. E. M. Adam, T. Johns, M. Sur, Dynamic control of visually guided locomotion through corticosubthalamic projections. *Cell Rep.* 40, 111139 (2022).

33. L. A. V. Magno, *et al.*, Optogenetic stimulation of the M2 cortex reverts motor dysfunction in a mouse model of Parkinson’s disease. *J. Neurosci.* 39, 3234–3248 (2019).

34. V. Gradinaru, M. Mogri, K. R. Thompson, J. M. Henderson, K. Deisseroth, Optical deconstruction of parkinsonian neural circuitry. *Science.* 324, 354–359 (2009).

35. L. A. Johnson, W. Xu, K. B. Baker, J. Zhang, J. L. Vitek, Modulation of motor cortex neuronal activity and motor behavior during subthalamic nucleus stimulation in the normal primate. *J. Neurophysiol.* 113, 2549–2554 (2015).

36. Q. Li, *et al.*, Therapeutic deep brain stimulation in parkinsonian rats directly influences motor cortex. *Neuron* 76, 1030–1041 (2012).

37. P. Payoux, *et al.*, Subthalamic nucleus stimulation reduces abnormal motor cortical overactivity in parkinson disease. *Arch. Neurol.* 61, 1307–1313 (2004).

38. T. H. Sanders, D. Jaeger, Optogenetic stimulation of cortico-subthalamic projections is sufficient to ameliorate bradykinesia in 6-ohda lesioned mice. *Neurobiol. Dis.* 95, 225–237 (2016).

39. S. Valverde, *et al.*, Deep brain stimulation-guided optogenetic rescue of parkinsonian symptoms. *Nat. Commun.* 11 (2020).

40. H. C. Pape, Queer current and pacemaker: the hyperpolarization-activated cation current in neurons. *Annu. Rev. Physiol.* 58, 299–327 (2003).

41. M. F. Nolan, J. T. Dudman, P. D. Dodson, B. Santoro, HCN1 channels control resting and active integrative properties of stellate cells from layer II of the entorhinal cortex. *J. Neurosci.* 27, 12440–12451 (2007).

42. R. B. Robinson, S. A. Siegelbaum, Hyperpolarization-activated cation currents: from molecules to physiological function. *Annu. Rev. Physiol.* 65, 453–480 (2003).

43. C. S. Chan, R. Shigemoto, J. N. Mercer, D. J. Surmeier, HCN2 and HCN1 channels govern the regularity of autonomous pacemaking and synaptic resetting in globus pallidus neurons. *J. Neurosci.* 24, 9921–9932 (2004).

44. Z. Huang, M. C. Walker, M. M. Shah, Loss of dendritic HCN1 subunits enhances cortical excitability and epileptogenesis. *J. Neurosci.* 29, 10979–10988 (2009).

45. J. C. Magee, Dendritic Ih normalizes temporal summation in hippocampal CA1 neurons. *Nat. Neurosci.* 2, 508–514 (1999).

46. S. P. Vaidya, D. Johnston, Temporal synchrony and gamma-to-theta power conversion in the dendrites of CA1 pyramidal neurons. *Nat. Neurosci. 2013 1612* 16, 1812–1820 (2013).

47. R. Narayanan, D. Johnston, The h channel mediates location dependence and plasticity of intrinsic phase response in rat hippocampal neurons. *J. Neurosci.* 28, 5846–5860 (2008).

48. F. G. Pike, *et al.*, Distinct frequency preferences of different types of rat hippocampal neurones in response to oscillatory input currents. *J. Physiol.* 529, 205–213 (2000).

49. H. Hu, K. Vervaeke, L. J. Graham, J. F. Storm, Complementary theta resonance filtering by two spatially segregated mechanisms in CA1 hippocampal pyramidal neurons. *J. Neurosci.* 29, 14472–14483 (2009).

50. H. G. Rotstein, *et al.*, Slow and fast inhibition and an H-current interact to create a theta rhythm in a model of CA1 interneuron network. *J. Neurophysiol.* 94, 1509–1518 (2005).

51. B. Marcelin, *et al.*, h channel-dependent deficit of theta oscillation resonance and phase shift in temporal lobe epilepsy. *Neurobiol. Dis.* 33, 436–447 (2009).

52. X. Shi, *et al.*, Behavioral assessment of sensory, motor, emotion, and cognition in rodent models of intracerebral hemorrhage. *Front. Neurol.* 12, 975 (2021).

53. N. A. Noor, H. S. Mohammed, I. M. Mourad, Y. A. Khadrawy, H. S. Aboul Ezz, A promising therapeutic potential of cerebrolysin in 6-OHDA rat model of Parkinson's disease. *Life Sci.* 155, 174–179 (2016).

54. M. Darvas, C. W. Henschen, R. D. Palmiter, Contributions of signaling by dopamine neurons in dorsal striatum to cognitive behaviors corresponding to those observed in Parkinson's disease. *Neurobiol. Dis.* 65, 112 (2014).

55. P. Brown, Abnormal oscillatory synchronisation in the motor system leads to impaired movement. *Curr. Opin. Neurobiol.* 17, 656–664 (2007).

56. L. Madisen, *et al.*, A toolbox of Cre-dependent optogenetic transgenic mice for light-induced activation and silencing. *Nat. Neurosci. 2012 155* 15, 793–802 (2012).

57. D. G. R. Tervo, *et al.*, A designer AAV variant permits efficient retrograde access to projection neurons. *Neuron* 92, 372 (2016).

58. J. M. Shine, *et al.*, Abnormal patterns of theta frequency oscillations during the temporal evolution of freezing of gait in Parkinson's disease. *Clin. Neurophysiol.* 125, 569–576 (2014).

59. H. Tan, *et al.*, Complementary roles of different oscillatory activities in the subthalamic nucleus in coding motor effort in Parkinsonism. *Exp. Neurol.* 248, 187–195 (2013).

60. J. S. Schor, *et al.*, Therapeutic deep brain stimulation disrupts movement-related subthalamic nucleus activity in parkinsonian mice. *Elife* 11 (2022).

61. T. Chomiak, B. Hu, Axonal and somatic filtering of antidromically evoked cortical excitation by simulated deep brain stimulation in rat brain. *J. Physiol.* 579, 403 (2007).

62. S. L. Jackman, B. M. Beneduce, I. R. Drew, W. G. Regehr, Achieving high-frequency optical control of synaptic transmission. *J. Neurosci.* 34, 7704–7714 (2014).

63. A. R. Aron, *et al.*, Converging evidence for a fronto-basal-ganglia network for inhibitory control of action and cognition. *J. Neurosci.* 27, 11860–11864 (2007).

64. A. D. Dorval, A. M. Kuncel, M. J. Birdno, D. A. Turner, W. M. Grill, Deep brain stimulation alleviates parkinsonian bradykinesia by regularizing pallidal activity. *J. Neurophysiol.* 104, 911–921 (2010).

65. R. Levy, *et al.*, Dependence of subthalamic nucleus oscillations on movement and dopamine in Parkinson's disease. *Brain* 125, 1196–1209 (2002).

66. J. Wagner, J. R. Wessel, A. Ghahremani, A. R. Aron, Establishing a right frontal beta signature for stopping action in scalp EEG: implications for testing inhibitory control in other task contexts. *J. Cogn. Neurosci.* 30, 107 (2018).

67. S. J. Thuault, *et al.*, Prefrontal cortex HCN1 channels enable intrinsic persistent neural firing and executive memory function. *J. Neurosci.* 33, 13583–13599 (2013).

68. Y. S. Yang, S. J. Son, J. H. Choi, J. C. Rah, Synaptic transmission and excitability during hypoxia with inflammation and reoxygenation in hippocampal CA1 neurons. *Neuropharmacology* 138, 20–31 (2018).

69. A. Devergnas, D. Pittard, D. Bliwise, T. Wichmann, Relationship between oscillatory activity in the cortico-basal ganglia network and parkinsonism in MPTP-treated monkeys. *Neurobiol. Dis.* 68, 156–166 (2014).

70. A. Leblois, *et al.*, Late emergence of synchronized oscillatory activity in the pallidum during progressive parkinsonism. *Eur. J. Neurosci.* 26, 1701–1713 (2007).

71. K. Niyomrat, D. Cheaha, J. Nukitram, E. Kumarnsit, Locomotor activity and resting local field potential oscillatory rhythms of 6-OHDA mouse model of Parkinson's disease in response to acute and repeated treatments with L-dopa. *Neurosci. Lett.* 759, 136007 (2021).

72. J. Soares, *et al.*, Role of external pallidal segment in primate parkinsonism: comparison of the effects of 1-methyl-4-phenyl-1,2,3,6-tetrahydropyridine-induced parkinsonism and lesions of the external pallidal segment. *J. Neurosci.* 24, 6417–6426 (2004).

73. E. Stein, I. Bar-Gad, Beta oscillations in the cortico-basal ganglia loop during parkinsonism. *Exp. Neurol.* 245, 52–59 (2013).

74. J. Wang, *et al.*, Network-wide oscillations in the parkinsonian state: Alterations in neuronal activities occur in the premotor cortex in parkinsonian nonhuman primates. *J. Neurophysiol.* 117, 2242–2249 (2017).

75. M. Moazami-Goudarzi, J. Sarnthein, L. Michels, R. Moukhtieva, D. Jeanmonod, Enhanced frontal low and high frequency power and synchronization in the resting EEG of parkinsonian patients. *Neuroimage* 41, 985–997 (2008).

76. A. Morita, S. Kamei, K. Serizawa, T. Mizutani, The relationship between slowing EEGs and the progression of Parkinson's disease. *J. Clin. Neurophysiol.* 26, 426–429 (2009).

77. D. Stoffers, *et al.*, Slowing of oscillatory brain activity is a stable characteristic of Parkinson's disease without dementia. *Brain* 130, 1847–1860 (2007).

78. W. D. Hutchison, A. M. Lozano, R. R. Tasker, A. E. Lang, J. O. Dostrovsky, Identification and characterization of neurons with tremor-frequency activity in human globus pallidus. *Exp. Brain Res. 1997 1133* 113, 557–563 (1997).

79. J. Kim, *et al.*, Dopamine depletion can be predicted by the aperiodic component of subthalamic local field potentials. *Neurobiol. Dis.* 168, 105692 (2022).

80. G. Paxinos, K. B. J. Franklin, The mouse brain in stereotaxic coordinates, 5th edition. *Acad. Press*, plate 45-47. (2019).

81. E. M. Dastin-van Rijn, *et al.*, Uncovering biomarkers during therapeutic neuromodulation with PARRM: Period-based artifact reconstruction and removal method. *Cell Reports Methods* 1, 100010 (2021).

82. F. J. Chaure, H. G. Rey, R. Quian Quiroga, A novel and fully automatic spike-sorting implementation with variable number of features. *J. Neurophysiol.* 120, 1859–1871 (2018).

83. T. Donoghue, *et al.*, Parameterizing neural power spectra into periodic and aperiodic components. *Nat. Neurosci.* 23, 1655–1665 (2020).

84. M. Gerster, *et al.*, Separating neural oscillations from aperiodic 1/f activity: challenges and recommendations. *Neuroinformatics* 20, 991–1012 (2022)

**Figure legends**

**Fig. 1. Effect of the 6-OHDA lesion on M2 activity. A.** Schematic diagram of the site of stereotaxic injection in the medial forebrain bundle (MFB) connecting the striatum and the substantia nigra pars compacta (SNc) and in-vivo experimental set-up. The 6-hydroxydopamine (6-OHDA) is injected into the MFB of Ai27D (Rosa-CAG-LSL-hChR2(H134R)-tdTomato-WPR) mice. **B.** Raster plots of representative single-unit activity recorded in premotor cortex (M2) of control and Parkinson's disease mouse models. **C-E.** Population average firing rate (left), burst duration (middle), and spikes in a burst (right) in control (n = 54 neurons) and 6-hydroxydopamine (6-OHDA)-lesioned mice (n = 168 neurons). Spontaneous single-unit activity in the M2 is higher in 6-OHDA-lesioned mice than in control mice (firing rate, $p = 0.053$; burst duration, $p = 0.84$; averaged number of activities in a burst, $^*p = 0.033$, Mann–Whitney test). **F.** Representative graph of whole-cell patch-clamp recording of M2 layer 5 pyramidal neurons. **G-H.** Representative traces in the whole-cell current clamp recording in M2 layer 5 pyramidal neurons following current injection with control (blue) and 6-OHDA lesion (orange) and the frequency-current relationship from control and 6-OHDA lesion mice. **I-M.** Summarized results showing similar resting membrane potential (I) and threshold (J), a decreased rheobase (K), an increased input resistance (L) and an increased voltage sag (M) in control mice and 6-OHDA lesioned mice. Data are presented as mean ± standard deviation.

**Fig. 2. Neurons in the M2 are synaptically connected with the subthalamic nucleus (STN).** **A.** Schematic diagram for visualizing subthalamic nucleus STN-projecting neurons with rAAV-retro. The viral vector rAAV-retro-Ef1a-mCherry-IRES-Cre (≥ $7\times10^{12}$ vig/mL) is injected into the STN of Ai27D (Rosa-CAG-LSL-hChR2(H134R)-tdTomato-WPR) mice. **B.** A representative image of rAAV-retro-labeled STN-projecting neurons in a 50 μm brain slice (left, scale bar = 500 μm) and a zoomed-in image of the boxed area (right, scale bar = 200 μm). M1: primary motor cortex; ACC, anterior cingulate cortex; PrL, prelimbic cortex. **C.** Schematic diagram of the in vivo recording setup. **D.** Raster plot (top) and averaged multiunit activity normalized to the mean baseline (middle and bottom) in response to 140 Hz electrical stimulation in the STN.

**Fig. 3. Wire hanging test and gait analysis of PD mouse models upon optogenetic stimulation of STN-projecting M2 neurons. A.** Schematic of selective STN-projecting M2 neuron stimulation. **B.** Mean wire-hanging time of PD model mice before and after optogenetic M2 stimulation. Optogenetic stimulation significantly increases the hanging time in the wire hanging test (473 nm, 9 mW/mm$^2$, 2 msec square pulses at 140 Hz, n = 7, $p = 0.026$, paired t-test). **C.** Representative positions of the paws extracted from the ventral plane videography. PD mouse model before (orange) and after (green) optogenetic stimulation. **D.** Paw area with the left hind limb in contact with the treadmill surface before (orange) and after (green) optogenetic stimulation in 6-OHDA lesioned mice. **E.** Comparison of gait parameters (stance time, stride time, stride length, stride frequency, coefficient of variation (CV) of the paw area, and paw angle) of the paws with the left hind limb of 6-OHDA lesioned mice before and after optogenetic stimulation (****$p<0.001$, **$p<0.01$, *$p<0.05$ relative to 6-OHDA lesioned mice; paired t-test, n =14). Data are presented as box and whisker plots, where each dot represents the mean before and after optogenetic stimulation.

**Fig. 4. Pattern and frequency of single unit activities measured in the M2. A.** Example raster plots of representative single units with optogenetic stimulation. **B**. Schematic diagram of the in vivo recording setup. **C-E**. Frequency (C), burst duration (E), and the number of units in a burst (F) in M2 activity upon optogenetic stimulation (n= 121 neurons, $^{***}p < 0.001$, $^{**}p < 0.01$, $^{*}p < 0.05$, paired t-test). **F.** Averaged unit counts binned for 20 s from a PD mouse model (n = 121, 19 mice). Unit counts at baseline, during, and after stimulation are color-coded as orange, light green, and dark green, respectively. The superimposed line plots illustrate that the number of units increases (black, n = 59 neurons) or decreases (red, n = 62 neurons) after optogenetic stimulation. Note that the units that decrease by stimulation show a high baseline firing rate. **G.** Baseline unit counts grouped according to the direction of the frequency changes. The baseline activity of M2 neurons is higher in the inhibited (n = 62 neurons) than the activated (n = 59 neurons) neurons after optogenetic stimulation (p = 0.015, Mann–Whitney test).

**Fig. 5. Frequency of single units recorded in the M2 in response to high-frequency electrical STN stimulation. A**. Schematic diagram of the in vivo recording setup. **B-C.** Raster plot (upper) and its 4.5-s time-binned histogram (lower) of three representative single units in the M2 for 6-OHDA (B, n = 16) and sham control (C, n = 35) mice. The firing rates are normalized to the mean firing of the baseline activities. **D-E.** Moving averaged (5-s time window without overlapping) firing rate of all single units measured from 16 OHDA-lesioned mice (D) and 35 sham control mice (E). The firing rate is normalized to the mean firing rate before the stimulation. The dashed gray line describes the mean value of the normalized firing rates before stimulation. The solid lines represent the average firing rates. The shaded area represents the standard error of the mean for all units for each condition. **F**. Violin plots of firing rate ratio before and after stimulation. A single scatter represents the firing rate of a single unit using a natural logarithm. The thick vertical lines show the first and third quartiles, whereas the thin vertical lines display 95% confidence intervals. The white dots and thick horizontal lines represent the median and mean values, respectively (n = 16, PD model and n = 35, control; ** $p<0.01$, unpaired *t*-test).

**Fig. 6. Intrinsic excitability of M2 neurons upon optogenetic stimulation in the PD mouse model. A.** Example voltage traces of M2 neurons in 6-OHDA mice in response to depolarizing current injections at -200 and 350 pA amplitudes. **B.** Mean firing frequencies of 50-350 pA depolarizing step current injections before (orange) and after (green) optogenetic stimulation. **C.** Resting membrane potentials (-79.49 ± 1.44 mV before stimulation vs. -75.24 ± 1.92 mV after stimulation, n = 18, p = 0.014, paired t-test). **D.** Action potential threshold (-40.36 ± 1.14 mV before and -39.35 ± 1.38 mV after stimulation, n = 18, p = 0.19, paired t-test). **E.** The minimum current required for evoking an action potential, rheobase (66.66 ± 9.90 pA before and 113.88 ± 16.57 pA after stimulation, n = 18, p = 0.002, paired t-test), **F.** Input resistance (before stimulation, 159.12 ± 8.13 mV vs. 134.15 ± 7.52 mV after optogenetic stimulation, n = 18, p = 0.0005, paired t-test), and **G.** voltage sag (4.90 ± 0.53 mV before and 3.46 ± 0.62 mV after stimulation, n = 18, p = 0.0018, paired t-test). Data are presented as box and whisker plots, where each graph shows the mean before and after optogenetic stimulation.

**Fig. 7. Effects of ZD7288 microinjection into M2 on the motor abnormalities in the PD mouse model. A.** Schematic illustration of the experiment. **B.** Mean wire-hanging time of control, PD model mice before and after ZD7288 administration. Wire-hanging time is increased after microinjection of ZD7288 in the PD mouse model (n = 12, $p = 0.031$, paired t-test). **C-H**. Comparison of gait parameters (swing time, stance time, stride time, stride length, stride frequency, coefficient of variation (CV) of the paw area) of the paws with the left hind limb of 6-OHDA lesioned mice before and after ZD7288 administration (**p<0.01, *p<0.05 relative to 6-OHDA lesioned mice; paired t-test, n =7). Data are presented as box and whisker plots, where each box represents the mean before and after ZD7288 administration.

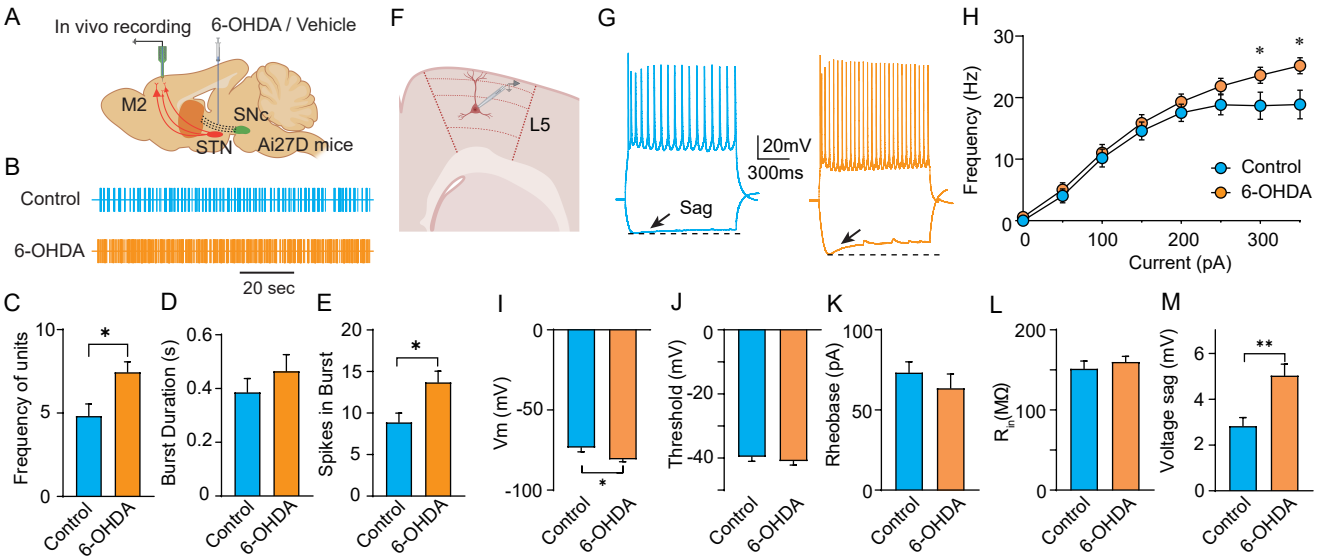
A
In vivo recording
6-OHDA / Vehicle
M2
SNc
STN
Ai27D mice
B
Control
6-OHDA
20 sec
F
L5
G
20mV
300ms
Sag
H
Frequency (Hz)
Current (pA)
Control
6-OHDA
C
Frequency of units
D
Burst Duration (s)
E
Spikes in Burst
I
Vm (mV)
J
Threshold (mV)
K
Rheobase (pA)
L
$R_{in}$ (MΩ)
M
Voltage sag (mV)
Control
6-OHDA

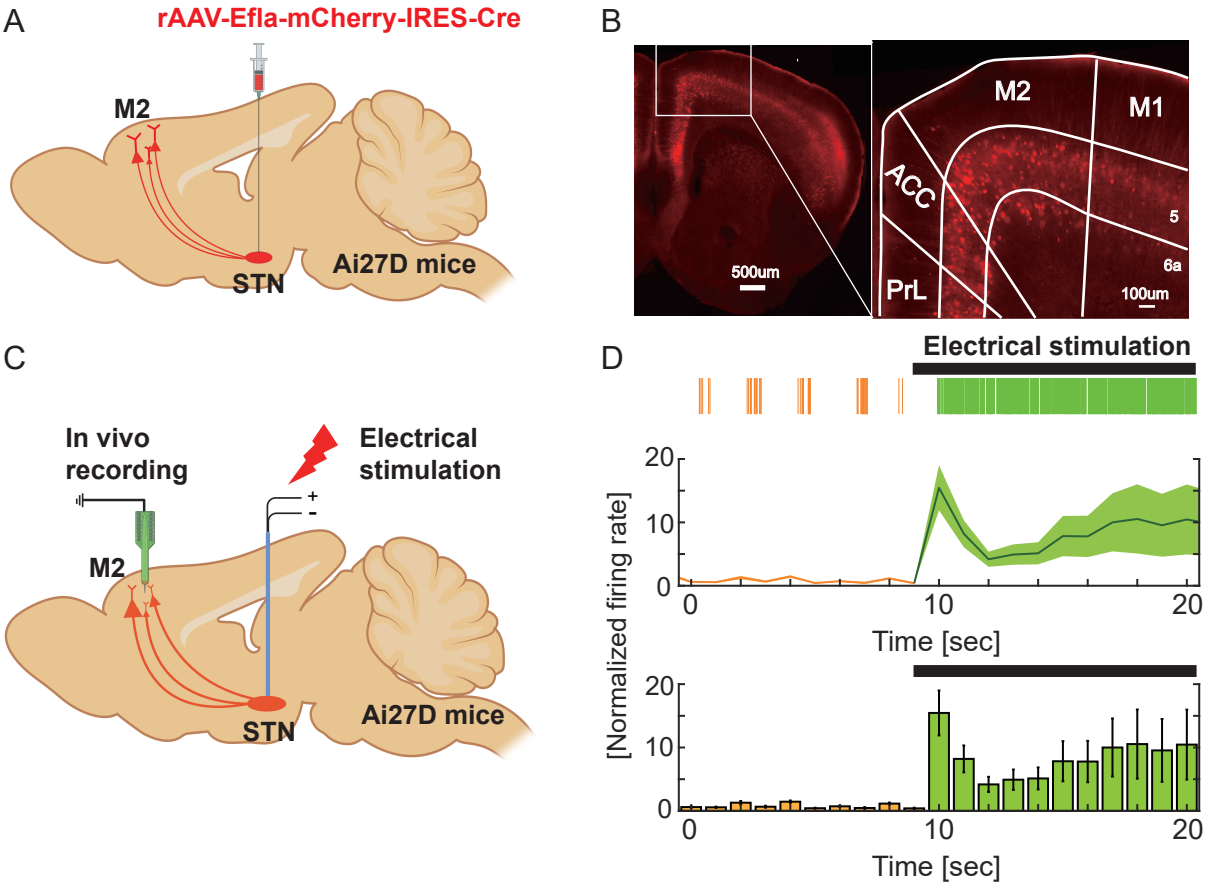
A
rAAV-Efla-mCherry-IRES-Cre
M2
STN
Ai27D mice
B
M2
M1
ACC
PrL
5
6a
500um
100um
C
In vivo recording
Electrical stimulation
M2
STN
Ai27D mice
D
Electrical stimulation
[Normalized firing rate]
Time [sec]
Time [sec]

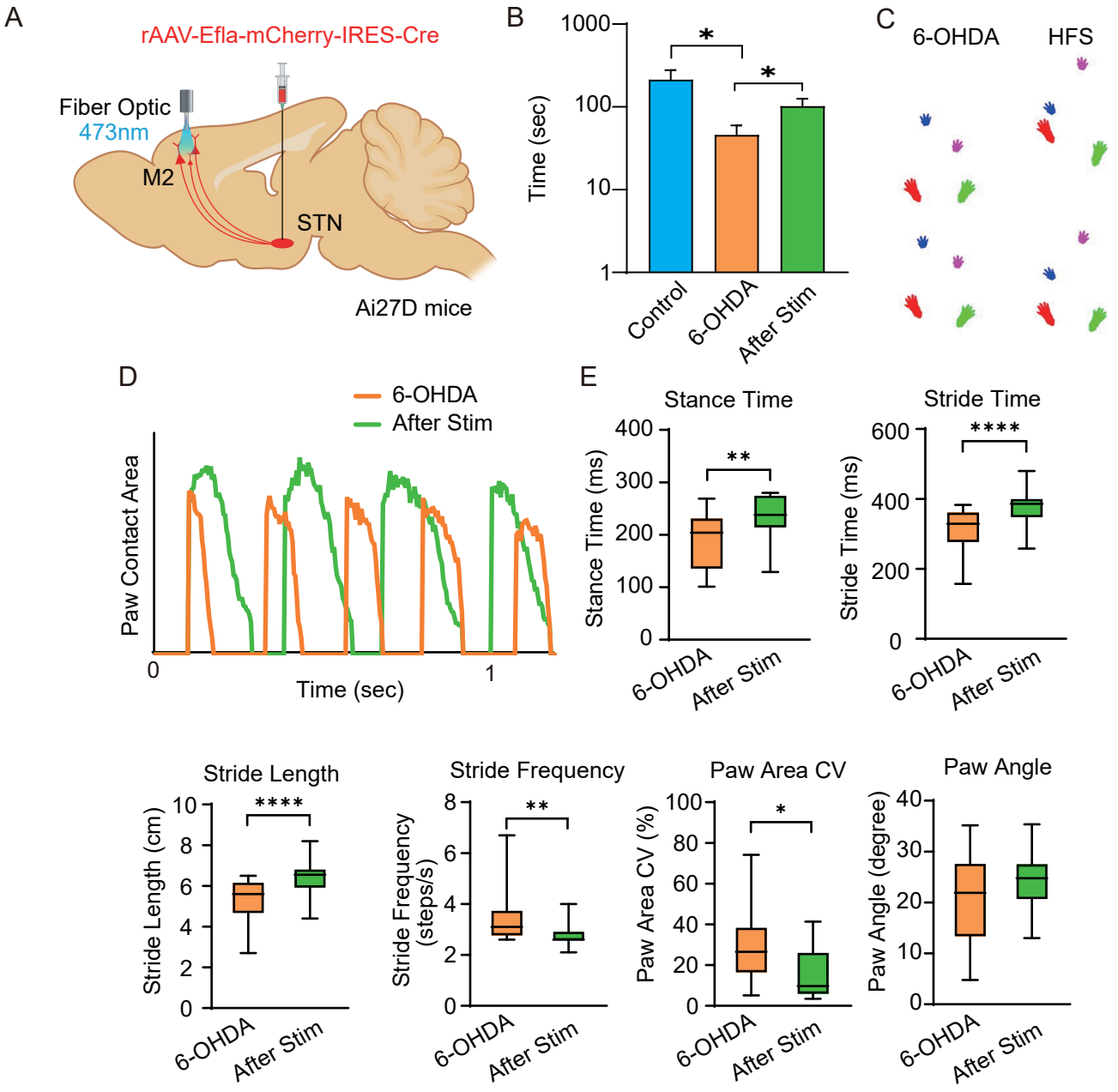
A
rAAV-Efla-mCherry-IRES-Cre
Fiber Optic
473nm
M2
STN
Ai27D mice
B
Time (sec)
1000
100
10
1
*
*
Control
6-OHDA
After Stim
C
6-OHDA
HFS
D
6-OHDA
After Stim
Paw Contact Area
0
1
Time (sec)
E
Stance Time
Stance Time (ms)
400
300
200
100
0
**
6-OHDA
After Stim
Stride Time
Stride Time (ms)
600
400
200
0
****
6-OHDA
After Stim
Stride Length
Stride Length (cm)
10
8
6
4
2
0
****
6-OHDA
After Stim
Stride Frequency
Stride Frequency (steps/s)
8
6
4
2
0
**
6-OHDA
After Stim
Paw Area CV
Paw Area CV (%)
100
80
60
40
20
0
*
6-OHDA
After Stim
Paw Angle
Paw Angle (degree)
40
30
20
10
0
6-OHDA
After Stim

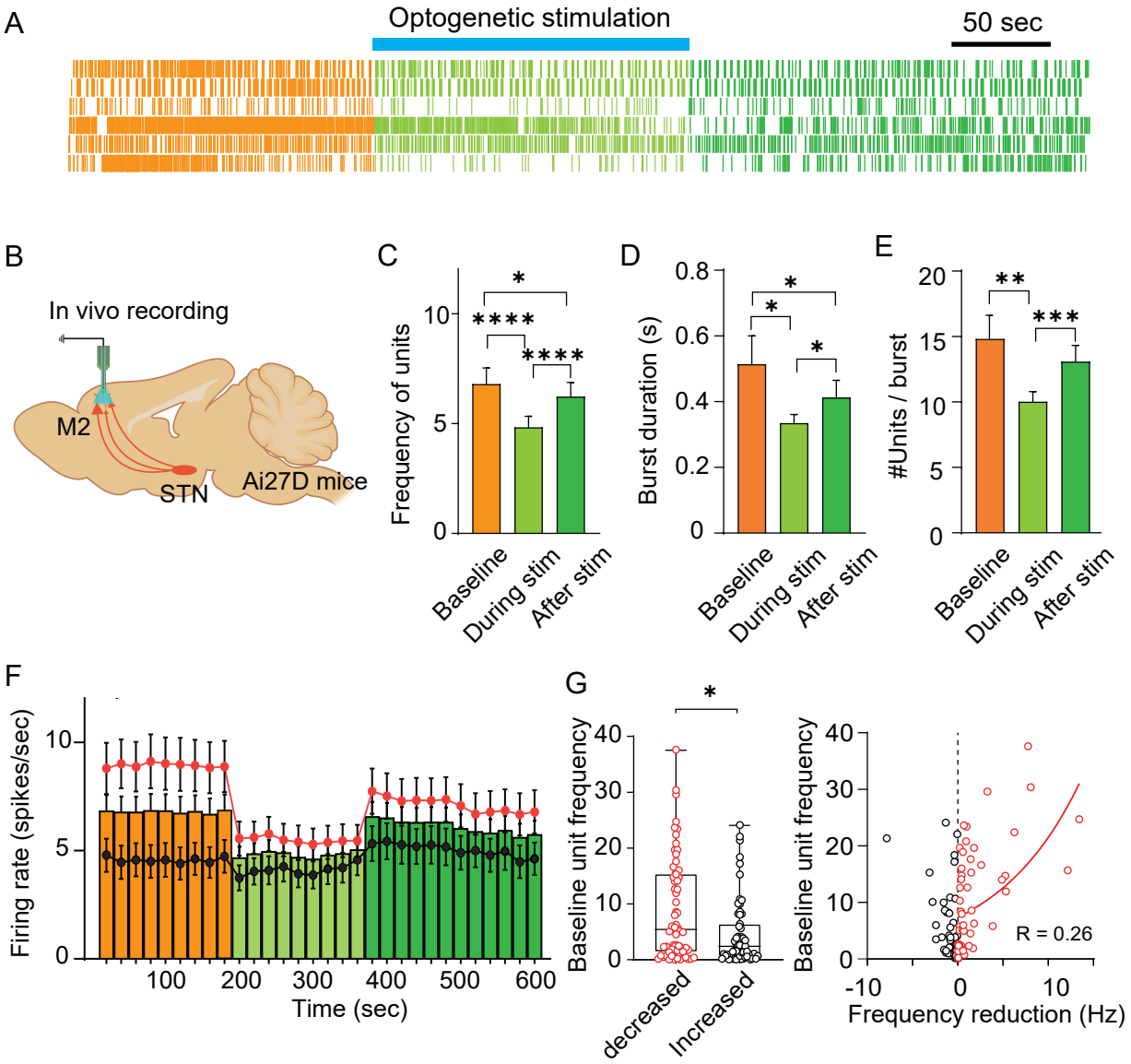
A
Optogenetic stimulation
50 sec
B
In vivo recording
M2
STN
Ai27D mice
C
Frequency of units
Baseline
During stim
After stim
D
Burst duration (s)
E
#Units / burst
F
Firing rate (spikes/sec)
Time (sec)
G
Baseline unit frequency
decreased
Increased
Frequency reduction (Hz)
R = 0.26

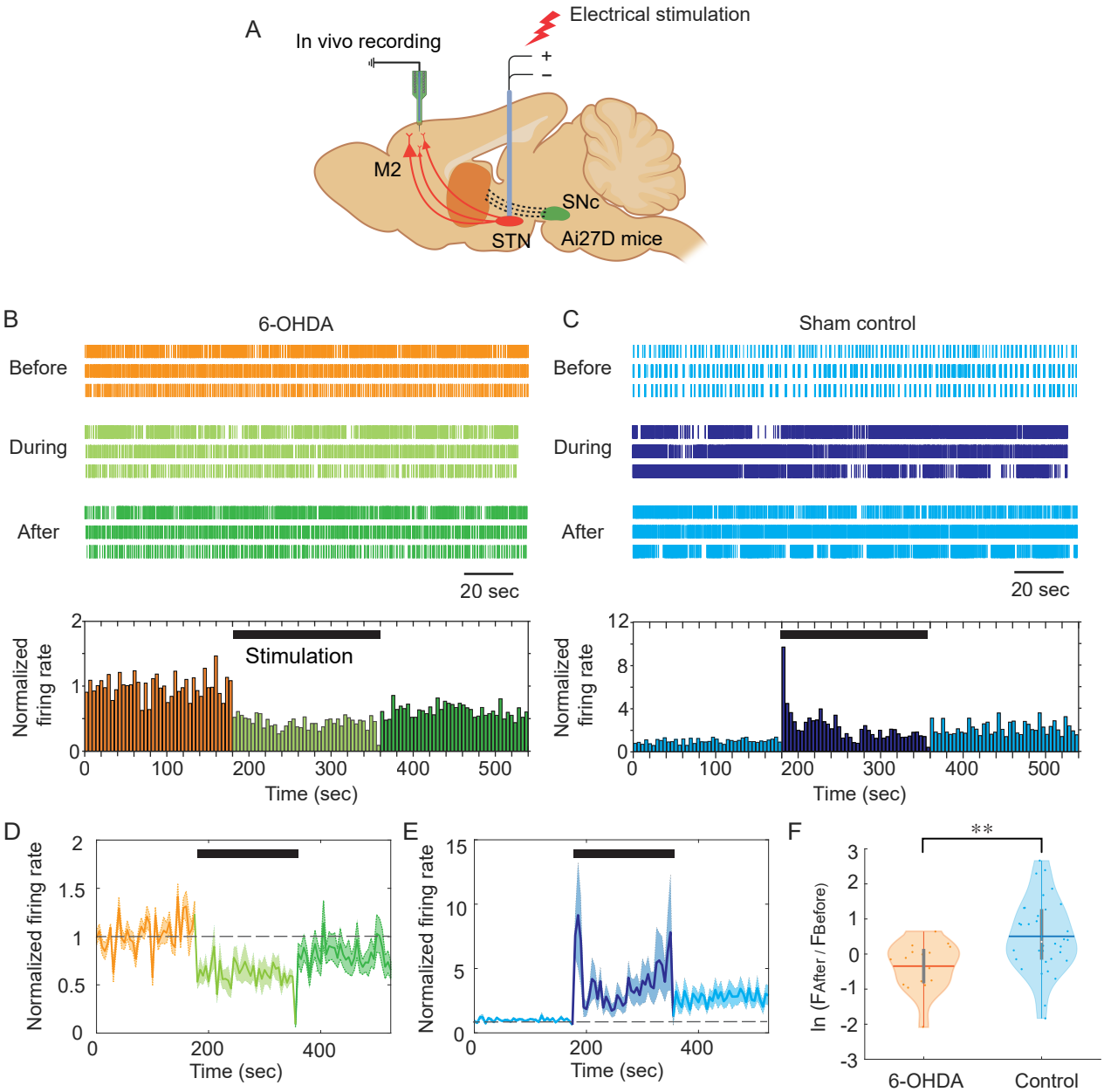
A
In vivo recording
Electrical stimulation
+
−
M2
SNc
STN
Ai27D mice
B
6-OHDA
Before
During
After
20 sec
Stimulation
Normalized firing rate
Time (sec)
C
Sham control
Before
During
After
20 sec
Normalized firing rate
Time (sec)
D
Normalized firing rate
Time (sec)
E
Normalized firing rate
Time (sec)
F
**
ln (FAfter / FBefore)
6-OHDA
Control

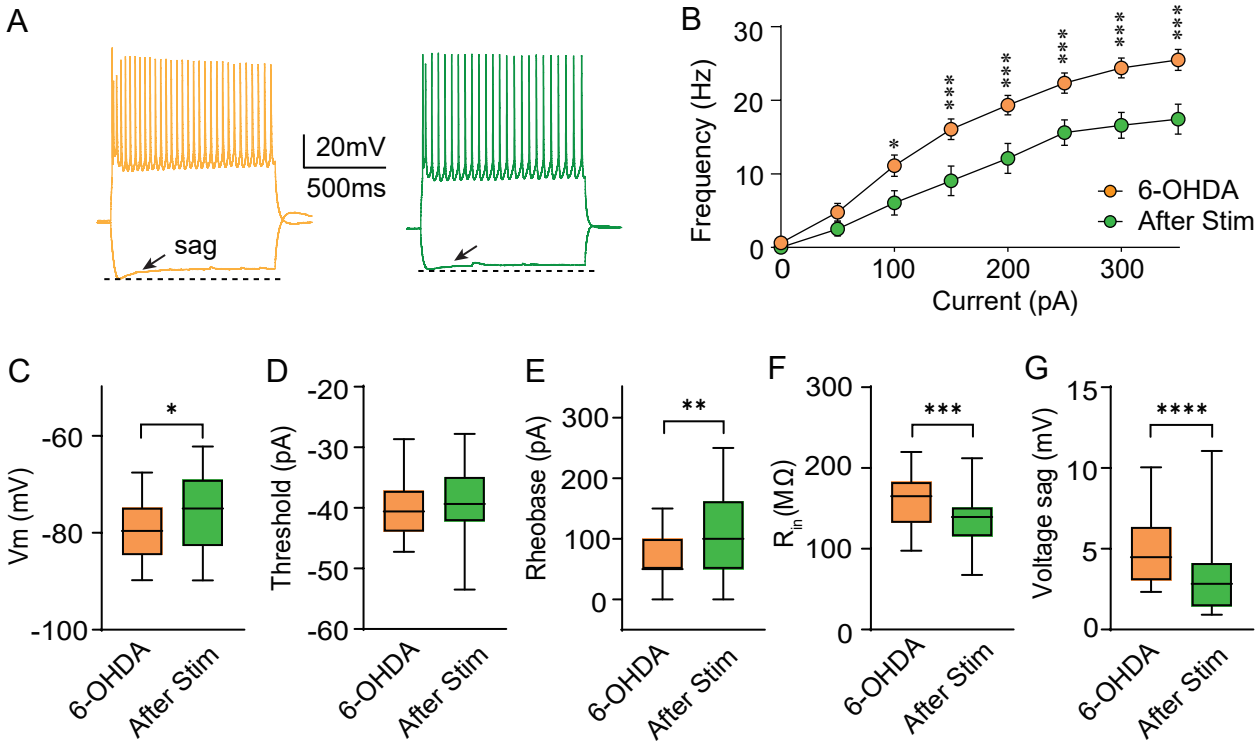
A
20mV
500ms
sag
B
Frequency (Hz)
Current (pA)
6-OHDA
After Stim
C
Vm (mV)
D
Threshold (pA)
E
Rheobase (pA)
F
$R_{in}$ (MΩ)
G
Voltage sag (mV)
6-OHDA
After Stim

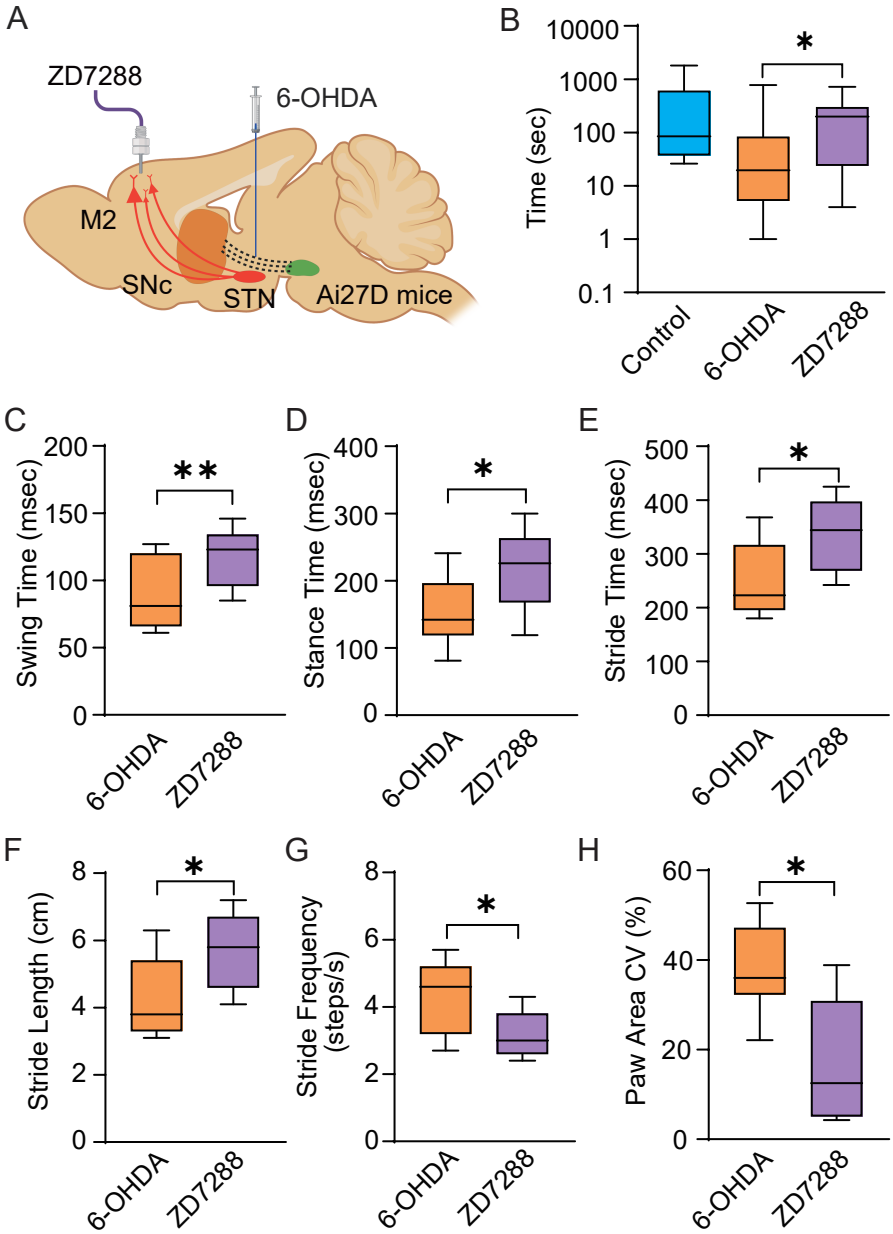
A
ZD7288
6-OHDA
M2
SNc
STN
Ai27D mice
B
Time (sec)
10000
1000
100
10
1
0.1
*
Control
6-OHDA
ZD7288
C
Swing Time (msec)
200
150
100
50
0
**
6-OHDA
ZD7288
D
Stance Time (msec)
400
300
200
100
0
*
6-OHDA
ZD7288
E
Stride Time (msec)
500
400
300
200
100
0
*
6-OHDA
ZD7288
F
Stride Length (cm)
8
6
4
2
0
*
6-OHDA
ZD7288
G
Stride Frequency (steps/s)
8
6
4
2
0
*
6-OHDA
ZD7288
H
Paw Area CV (%)
60
40
20
0
*
6-OHDA
ZD7288

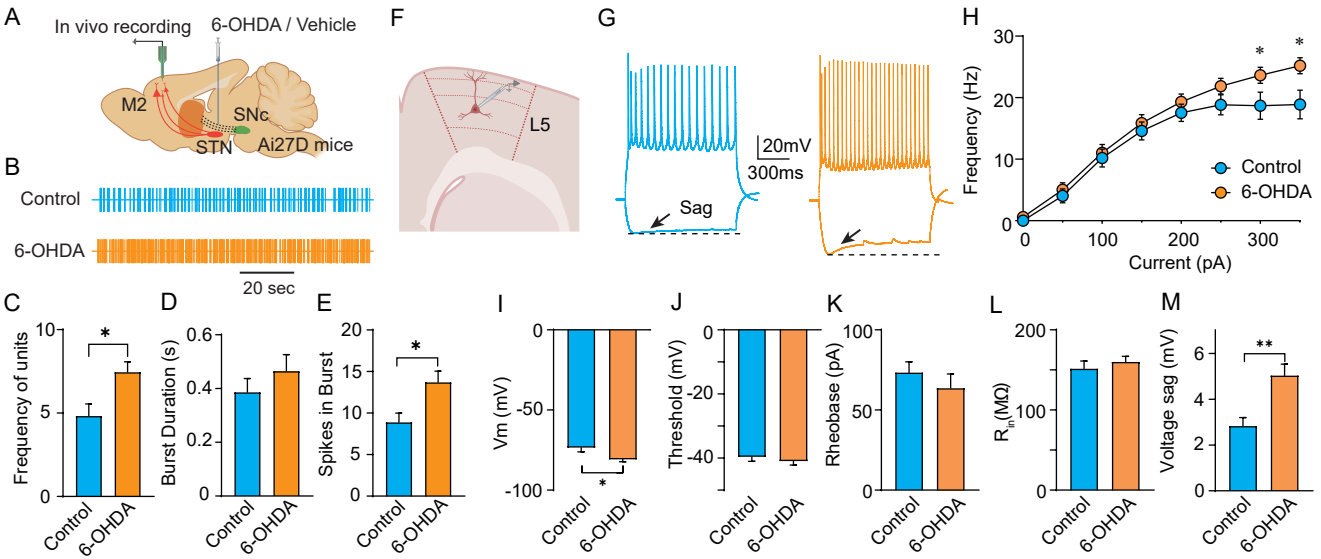
A
In vivo recording
6-OHDA / Vehicle
M2
SNc
STN
Ai27D mice
B
Control
6-OHDA
20 sec
F
L5
G
20mV
300ms
Sag
H
Frequency (Hz)
Current (pA)
Control
6-OHDA
C
Frequency of units
D
Burst Duration (s)
E
Spikes in Burst
I
Vm (mV)
J
Threshold (mV)
K
Rheobase (pA)
L
$R_{in}$ (MΩ)
M
Voltage sag (mV)
Control
6-OHDA

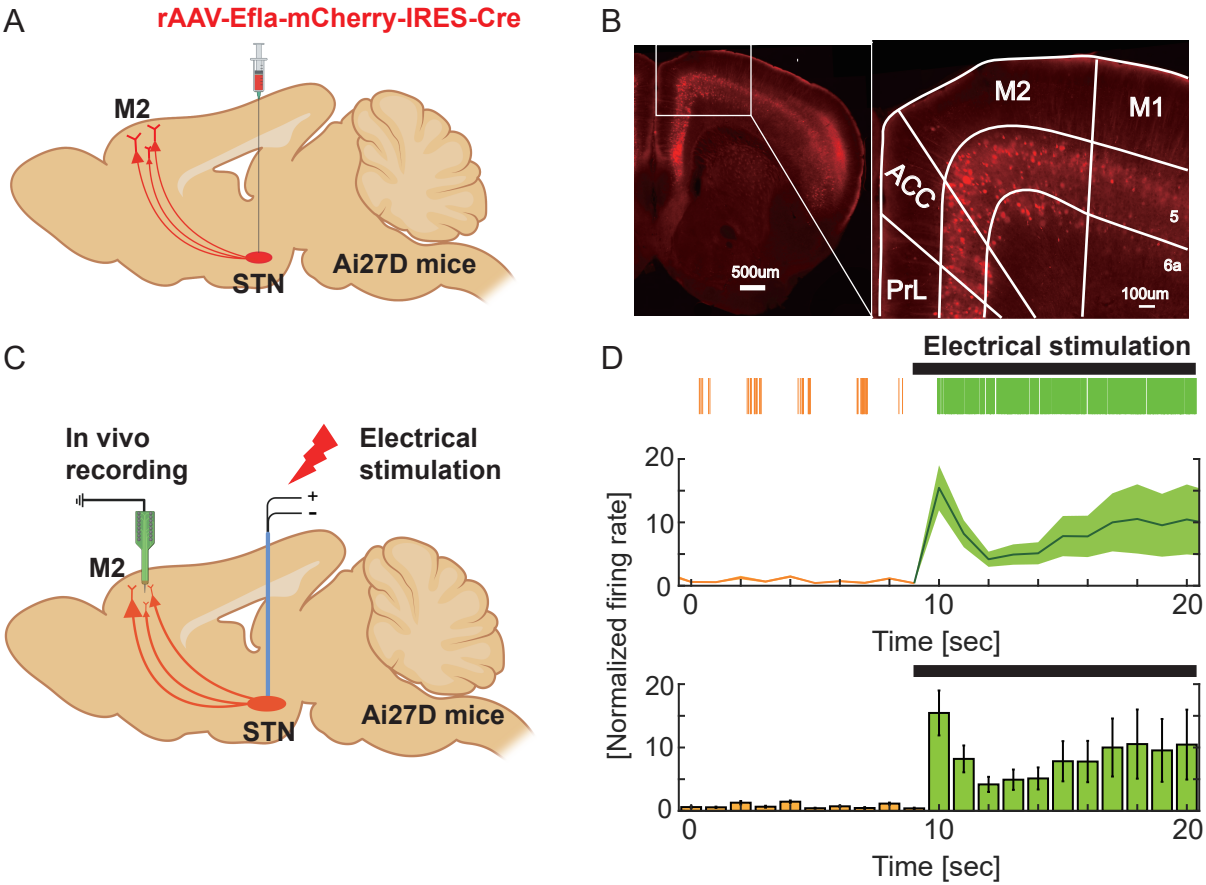
A
rAAV-Efla-mCherry-IRES-Cre
M2
STN
Ai27D mice
B
M2
M1
ACC
PrL
5
6a
500um
100um
C
In vivo recording
Electrical stimulation
M2
STN
Ai27D mice
D
Electrical stimulation
[Normalized firing rate]
Time [sec]
Time [sec]

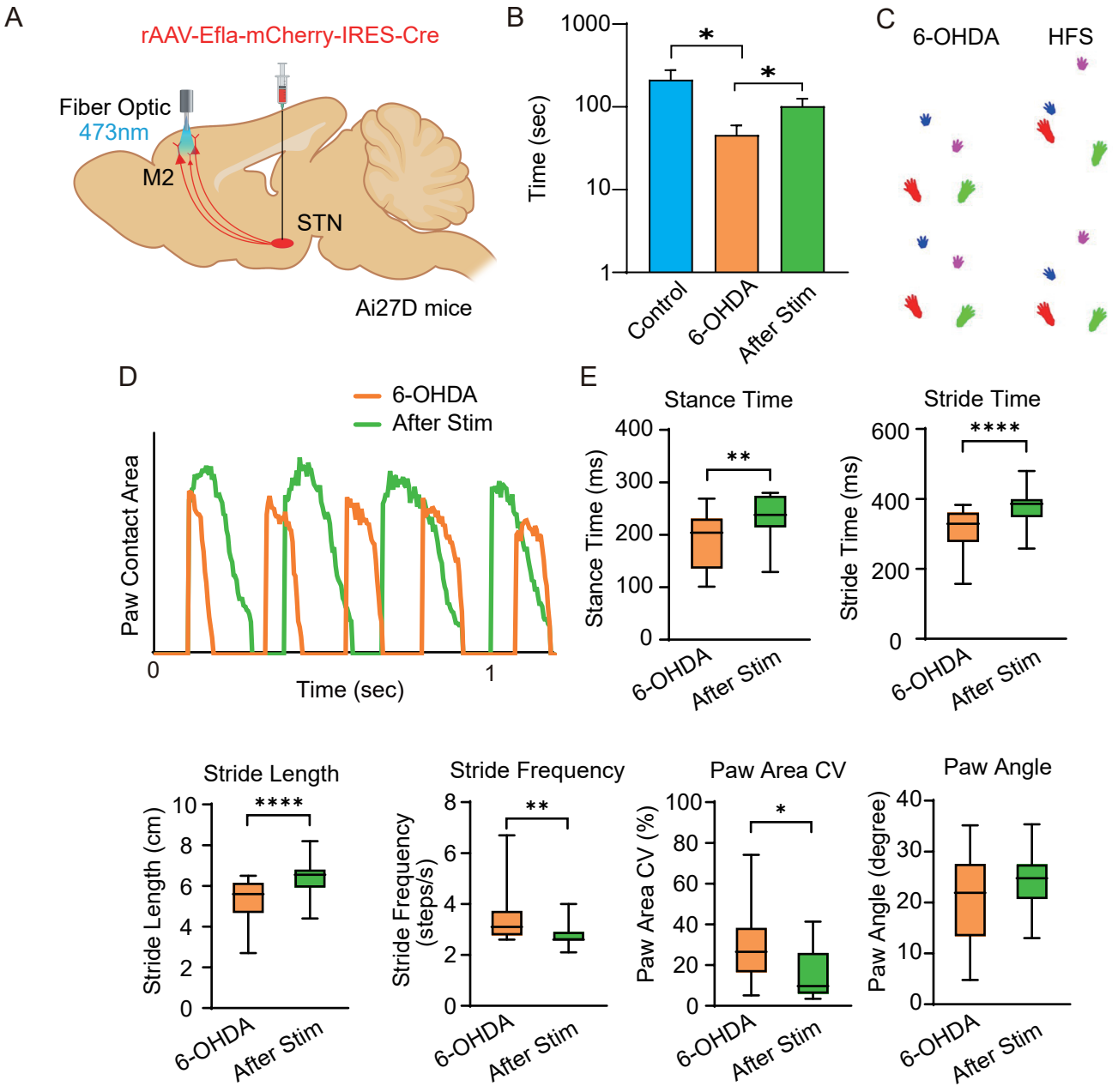
A
rAAV-Efla-mCherry-IRES-Cre
Fiber Optic
473nm
M2
STN
Ai27D mice
B
Time (sec)
1000
100
10
1
*
*
Control
6-OHDA
After Stim
C
6-OHDA
HFS
D
6-OHDA
After Stim
Paw Contact Area
0
1
Time (sec)
E
Stance Time
Stance Time (ms)
400
300
200
100
0
**
6-OHDA
After Stim
Stride Time
Stride Time (ms)
600
400
200
0
****
6-OHDA
After Stim
Stride Length
Stride Length (cm)
10
8
6
4
2
0
****
6-OHDA
After Stim
Stride Frequency
Stride Frequency (steps/s)
8
6
4
2
0
**
6-OHDA
After Stim
Paw Area CV
Paw Area CV (%)
100
80
60
40
20
0
*
6-OHDA
After Stim
Paw Angle
Paw Angle (degree)
40
30
20
10
0
6-OHDA
After Stim

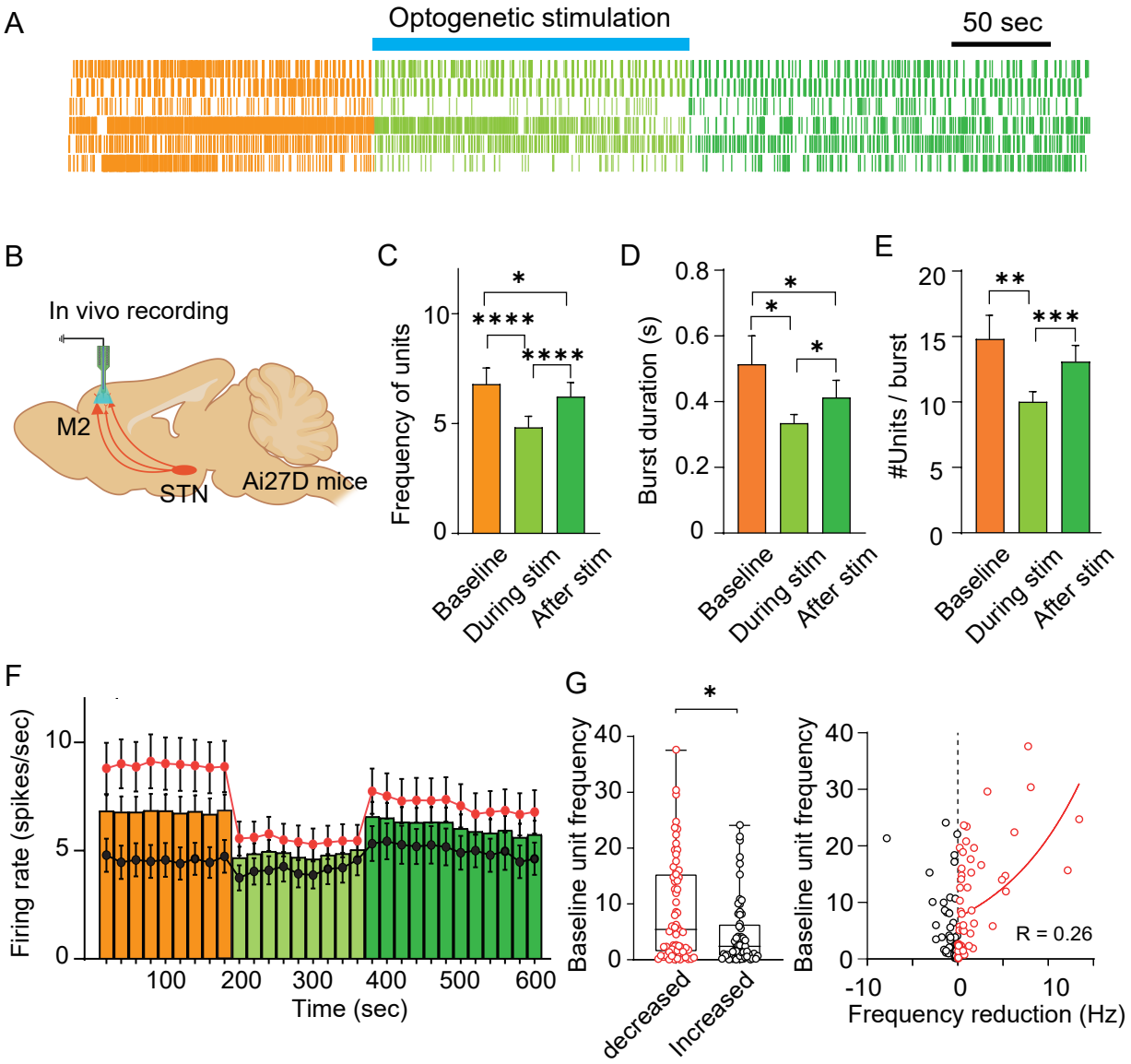
A
Optogenetic stimulation
50 sec
B
In vivo recording
M2
STN
Ai27D mice
C
Frequency of units
Baseline
During stim
After stim
D
Burst duration (s)
E
#Units / burst
F
Firing rate (spikes/sec)
Time (sec)
G
Baseline unit frequency
decreased
Increased
Frequency reduction (Hz)
R = 0.26

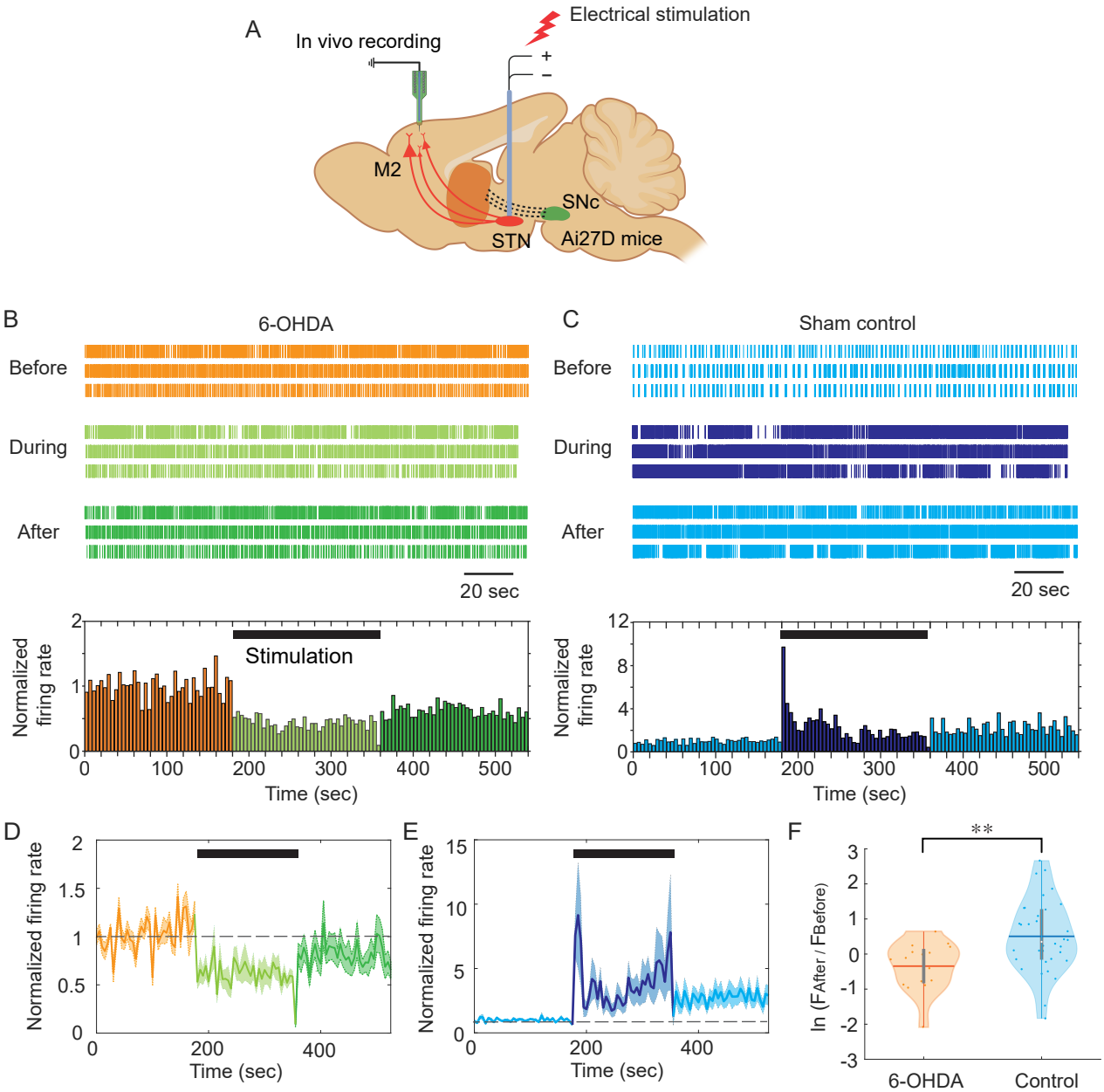
A
In vivo recording
Electrical stimulation
+
−
M2
SNc
STN
Ai27D mice
B
6-OHDA
Before
During
After
20 sec
Stimulation
Normalized firing rate
Time (sec)
C
Sham control
Before
During
After
20 sec
Normalized firing rate
Time (sec)
D
Normalized firing rate
Time (sec)
E
Normalized firing rate
Time (sec)
F
**
ln (FAfter / FBefore)
6-OHDA
Control

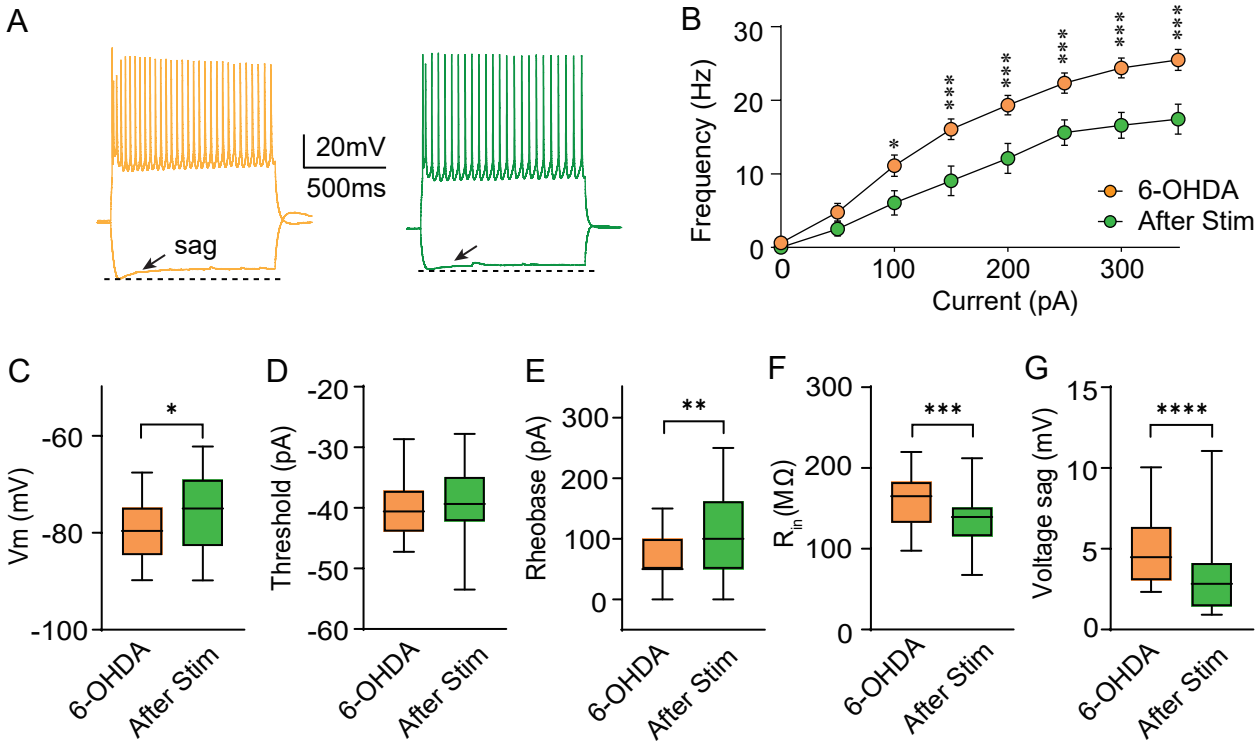
A
20mV
500ms
sag
B
Frequency (Hz)
Current (pA)
6-OHDA
After Stim
C
Vm (mV)
D
Threshold (pA)
E
Rheobase (pA)
F
$R_{in}$ (MΩ)
G
Voltage sag (mV)
6-OHDA
After Stim

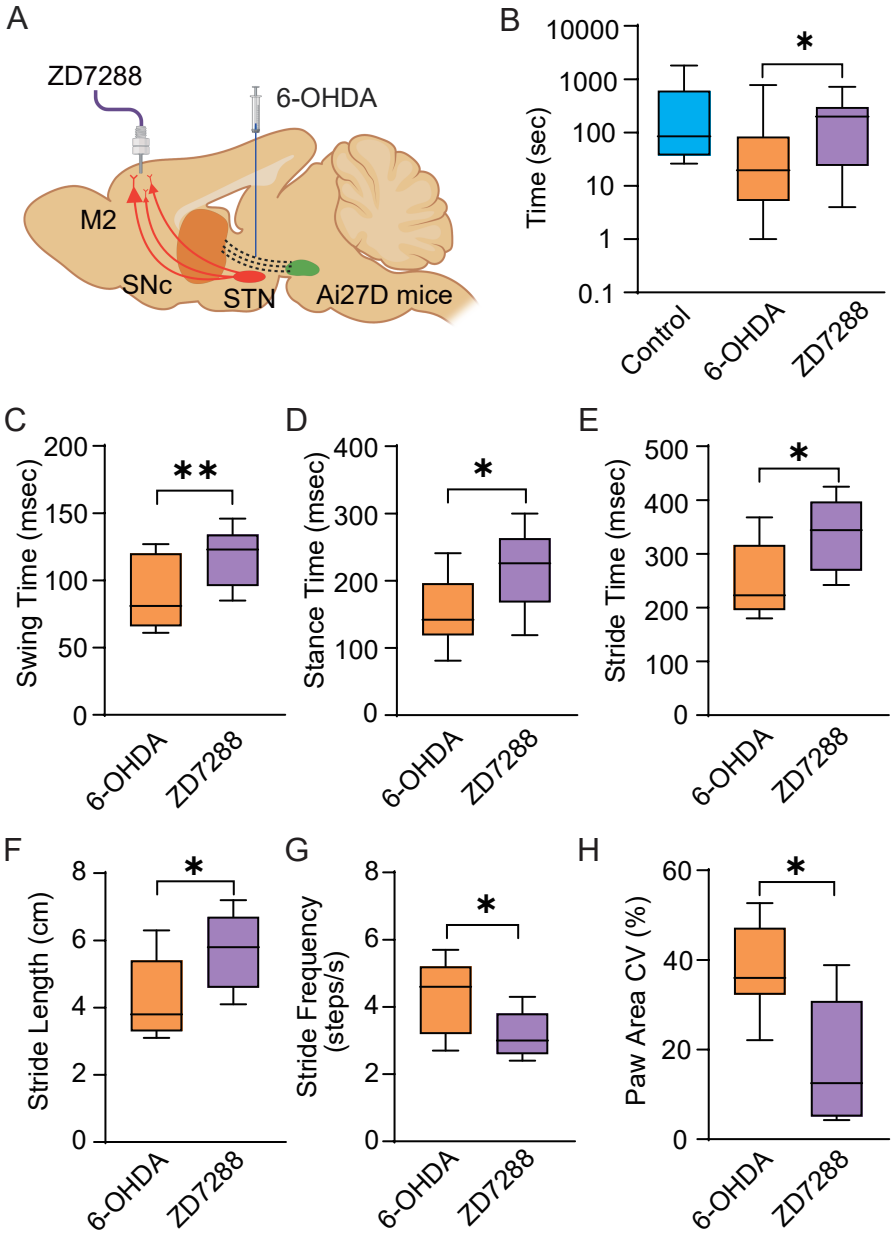
A
ZD7288
6-OHDA
M2
SNc
STN
Ai27D mice
B
Time (sec)
10000
1000
100
10
1
0.1
*
Control
6-OHDA
ZD7288
C
Swing Time (msec)
200
150
100
50
0
**
6-OHDA
ZD7288
D
Stance Time (msec)
400
300
200
100
0
*
6-OHDA
ZD7288
E
Stride Time (msec)
500
400
300
200
100
0
*
6-OHDA
ZD7288
F
Stride Length (cm)
8
6
4
2
0
*
6-OHDA
ZD7288
G
Stride Frequency (steps/s)
8
6
4
2
0
*
6-OHDA
ZD7288
H
Paw Area CV (%)
60
40
20
0
*
6-OHDA
ZD7288